

Evaluation of probabilistic photometric redshift estimation approaches for LSST

S.J. Schmidt¹, A.I. Malz^{2,3,4}, J.Y.H. Soo⁵, I.A. Almosallam^{6,7}, M. Brescia⁸, S. Cavaudi^{8,9}, J. Cohen-Tanugi¹⁰, A.J. Connolly¹¹, P.E. Freeman¹², M.L. Graham¹¹, K. Iyer¹³, M.J. Jarvis^{14,15}, J.B. Kalmbach¹⁶, E. Kovacs¹⁷, A.B. Lee¹², G. Longo⁹, C. B. Morrison¹¹, J. Newman¹⁸, E. Nourbakhsh¹, E. Nuss¹⁰, T. Pospisil¹², H. Tranin¹⁰, R. Zhou¹⁸, R. Izbicki^{19,20}

(LSST Dark Energy Science Collaboration)

¹ Department of Physics, University of California, One Shields Ave., Davis, CA, 95616, USA

² German Centre of Cosmological Lensing, Ruhr-Universitaet Bochum, Universitaetsstrasse 150, 44801 Bochum, Germany

³ Center for Cosmology and Particle Physics, New York University, 726 Broadway, New York, 10003, USA

⁴ Department of Physics, New York University, 726 Broadway, New York, 10003, USA

⁵ Department of Physics and Astronomy, University College London, Gower Street, London WC1E 6BT, UK

⁶ King Abdulaziz City for Science and Technology, Riyadh 11442, Saudi Arabia

⁷ Information Engineering, Parks Road, Oxford, OX1 3PJ, UK

⁸ INAF-Capodimonte Observatory, Salita Moiariello 16, I-80131, Napoli, Italy

⁹ Department of Physics E. Pancini, University Federico II, via Cinthia 6, I-80126, Napoli, Italy

¹⁰ Laboratoire Univers et Particules de Montpellier, Université de Montpellier, CNRS, Montpellier, France

¹¹ Department of Astronomy, University of Washington, Box 351580, U.W., Seattle WA 98195, USA

¹² Department of Statistics & Data Science, Carnegie Mellon University, 5000 Forbes Avenue, Pittsburgh, PA 15213, USA

¹³ Department of Physics and Astronomy, Rutgers, The State University of New Jersey, 136 Frelinghuysen Road, Piscataway, NJ 08854-8019 USA

¹⁴ Astrophysics, Department of Physics, University of Oxford, Denys Wilkinson Building, Keble Road, Oxford, OX1 3RH, UK

¹⁵ Department of Physics and Astronomy, University of the Western Cape, Bellville 7535, South Africa

¹⁶ Department of Physics, University of Washington, Box 351560, Seattle, WA 98195, USA

¹⁷ Argonne National Laboratory, Lemont, IL 60439, USA

¹⁸ Department of Physics and Astronomy and the Pittsburgh Particle Physics, Astrophysics and Cosmology Center (PITT PACC), University of Pittsburgh, Pittsburgh, PA 15260, USA

¹⁹ Department of Statistics, Federal University of Sao Carlos, Sao Carlos, Brazil

²⁰ External collaborator

10 September 2019

ABSTRACT

Many scientific investigations of photometric galaxy surveys require redshift estimates, whose uncertainty properties are best encapsulated by photometric redshift (photo- z) posterior probability distribution functions (PDFs). A plethora of photo- z PDF estimation methodologies abound, producing discrepant results with no consensus on a preferred approach. We present the results of a comprehensive experiment comparing twelve photo- z algorithms applied to mock data produced for the Large Synoptic Survey Telescope (LSST) Dark Energy Science Collaboration (DESC). By supplying perfect prior information, in the form of the complete template library and a representative training set as inputs to each code, we demonstrate the impact of the assumptions underlying each technique on the output photo- z PDFs. In the absence of a notion of true, unbiased photo- z PDFs, we evaluate and interpret multiple metrics of the ensemble properties of the derived photo- z PDFs as well as traditional reductions to photo- z point estimates. We report systematic biases and overall over/under-breadth of the photo- z PDFs of many popular codes, which may indicate avenues for improvement in the algorithms or implementations. Furthermore, we raise attention to the limitations of established metrics for assessing photo- z PDF accuracy; though we identify the conditional density estimate (CDE) loss as a promising metric of photo- z PDF performance in the case where true redshifts are available but true photo- z PDFs are not, we emphasize the need for science-specific performance metrics.

Key words: galaxies: distances and redshifts – galaxies: statistics – methods: statistical

2 LSST Dark Energy Science Collaboration

1 INTRODUCTION

The current and next generations of large-scale galaxy surveys, including the Dark Energy Survey (DES, Abbott et al. 2005), the Kilo-Degree Survey (KiDS, de Jong et al. 2013), Hyper Suprime-Cam Survey (HSC, Aihara et al. 2018a,b), Large Synoptic Survey Telescope (LSST, Abell et al. 2009), Euclid (Laureijs et al. 2011), and Wide-Field Infrared Survey Telescope (WFIRST, Green et al. 2012), represent a paradigm shift to reliance on photometric, rather than solely spectroscopic, galaxy catalogues of substantially larger size at a cost of lacking complete spectroscopically confirmed redshifts (z). Effective astrophysical inference using the catalogues resulting from these ongoing and upcoming missions, however, necessitates accurate and precise photometric redshift (photo- z) estimation methodologies.

As an example, in order for photo- z systematics to not dominate the statistical noise floor of LSST’s main cosmological sample of $\sim 10^7$ galaxies, the LSST Science Requirements Document (SRD)¹ specifies that individual galaxy photo- zs must have root-mean-square error $\sigma_z < 0.02(1+z)$, 3σ catastrophic outlier rate below 10%, and bias below 0.003. Specific science cases may have their own requirements on photo- z performance that exceed those of the survey as a whole. In that vein, the LSST Dark Energy Science Collaboration (LSST-DESC) developed a separate SRD (The LSST Dark Energy Science Collaboration et al. 2018) that conservatively forecasts the constraining power of five cosmological probes, leading to even more stringent requirements on photo- z performance, including those defined in terms of tomographically binned subsamples populations rather than individual galaxies.

Though the standard has long been for each galaxy in a photometric catalogue to have a photo- z point estimate and Gaussian error bar, even early applications of photo- zs in precision cosmology indicate the inadequacy of point estimates (Mandelbaum et al. 2008) to encapsulate the degeneracies resulting from the nontrivial mapping between broad band fluxes and redshift. Far from a hypothetical situation, such degeneracies are real consequences of the same deep imaging that enables larger galaxy catalogue sizes. The lower luminosity and higher redshift populations captured by deeper imaging introduce major physical systematics to photo- zs , among them the Lyman break/Balmer break degeneracy, that did not affect shallower large area surveys like the Sloan Digital Sky Survey (SDSS, York et al. 2000) and Two Micron All Sky Survey (2MASS, Skrutskie et al. 2006).

To fully characterize such physical degeneracies, later photometric galaxy catalogue data releases, (e. g. Sheldon et al. (2012); Erben et al. (2013); de Jong et al. (2017)), provide a more informative photo- z data product, the photo- z probability density function (PDF), that describes the redshift probability, commonly denoted as $p(z)$, as a function of a galaxy’s redshift, conditioned on the observed photometry. Early template-based methods such as Fernández-Soto et al. (1999) approximated the likelihood of photometry conditioned on redshift with the relative χ^2 values of template

spectra. Not long after, Bayesian adaptations of template-based approaches such as Benítez (2000) combined the estimated likelihoods with a prior to yield a posterior PDF of redshift conditioned on photometry. While the first data-driven photo- z algorithms yielded a point estimate, Firth et al. (2003) estimated a photo- z PDF using a neural net with realizations scattered within the photometric errors.

There are numerous techniques for deriving photo- z PDFs, yet no one method has been established as clearly superior. Consistent experimental conditions enable the quantification if not isolation of their differences, which can be interpreted as a sort of *implicit prior* imparted by the method itself. Comprehensive comparisons of photo- z methods have been made before; the Photo- z Accuracy And Testing (PHAT, Hildebrandt et al. 2010) effort focused on photo- z point estimates derived from many photometric bands. Rau et al. (2015) introduced a new method for improving photo- z PDFs using an ordinal classification algorithm. DES compared several codes for photo- z point estimates and a subset with photo- z PDF information (Sánchez et al. 2014) and examined summary statistics of photo- z PDFs for tomographically binned galaxy subsamples (Bonnett et al. 2016).

This paper is distinguished from other comparisons of photo- z methods by its focus on the evaluation criteria for photo- z PDFs and interpretation thereof. In the absence of simulated data drawn from known redshift distributions, the very concept of a “true PDF” for an individual galaxy is unavailable, and we must instead rely on measures of ensemble behaviour to characterize PDF quality (see § 4 for further discussion). We aim to perform a comprehensive sensitivity analysis of photo- z PDF techniques in order to ultimately select those that will become part of the LSST pipelines, as part of a key project of the Photometric Redshifts working group of the LSST-DESC, described in the Science Roadmap (SRM)². In this initial study, we focus on evaluating the performance of photo- z PDF codes using PDF-specific performance metrics in a formally controlled experiment with complete and representative prior information (template libraries and training sets) to set a baseline for subsequent investigations. This approach probes how each code considered exploits the information content of the data versus prior information from template libraries and training sets.

The outline of the paper is as follows: in § 2 we present the simulated data set; in § 3 we describe the current generation codes employed in the paper; in § 4 we discuss the interpretation of photo- z PDFs in terms of metrics of accuracy; in § 5 we show our results and compare the performance of the codes; in § 6 we offer our conclusions and discuss future extensions of this work.

2 DATA

In order to test the current generation of photo- z PDF codes, we employ an existing simulated galaxy catalogue, described in detail in Section 2.1. The experimental conditions shared

¹ available at <https://docushare.lsstcorp.org/docushare/dsweb/Get/LPM-17>

² Available at: http://lsst-desc.org/sites/default/files/DESC_SRMs_V1_1.pdf

among all codes are motivated by the LSST SRD requirements and implemented for machine learning and template-based photo- z PDF codes according to the procedures of Sections 2.3.1 and 2.3.2 respectively.

2.1 The Buzzard-v1.0 simulation

Our mock catalogue is derived from the BUZZARD-highres-v1.0 catalogue (DeRose et al. 2019, Wechsler et al., in prep.). BUZZARD is built on a dark matter-only N-body simulation of 2048^3 particles in a 400 Mpc h^{-1} box. The lightcone was constructed from smoothing and interpolation between a set of time snapshots. Dark matter halos were identified using the Rockstar software package (Behroozi et al. 2013) and then populated with galaxies with a stellar mass and absolute r -band magnitude in the SDSS system determined using a sub-halo abundance matching model constrained to match both projected two-point galaxy clustering statistics and an observed conditional stellar mass function (Reddick et al. 2013).

To assign a spectrum to each galaxy, the Adding Density Dependent Spectral Energy Distributions (SEDs) procedure (ADDSEDS, deRose in prep.)³ was used. ADDSEDS uses a sample of $\sim 5 \times 10^5$ galaxies from the magnitude-limited SDSS Data Release 6 Value Added Galaxy Catalogue (Blanton et al. 2005) to train an empirical relation between absolute r -band magnitude, local galaxy density, and SED. Each SDSS spectrum is parameterized by five weights corresponding to a weighted sum of five basis SED components using the k-correct software package⁴ (Blanton & Roweis 2007).

Correlations between SED and galaxy environment were included so as to preserve the colour-density relation of galaxy environment. The distance to the spatially projected fifth-nearest neighbour was used as a proxy for local density in the SDSS training sample. For each simulated galaxy, a galaxy with similar absolute r -band magnitude and local galaxy density was chosen from the training set, and that training galaxy's SED was assigned to the simulated galaxy.

2.1.1 Caveats

By necessity, BUZZARD does not contain all of the complicating factors present in real data, and here we discuss the most pertinent ways that these limitations affect our experiment. BUZZARD includes only galaxies, not stars nor AGN. The catalogue-based construction excludes image-level effects, such as deblending errors, photometric measurement issues, contamination from sky background (Zodiacal light, scattered light, etc.), lensing magnification, and Galactic reddening.

The BUZZARD SEDs are drawn from a set of $\sim 5 \times 10^5$ SEDs, which themselves are derived from a five-component linear combination fit to $\sim 5 \times 10^5$ SDSS galaxies; thus the sample contains only galaxies that resemble linear combinations of those for which SDSS obtained spectra, and there are necessarily duplicates. The linear combination SEDs also restrict the properties of the galaxy population to linear combinations of the properties corresponding to five basis

templates, precluding the modeling of non-linear features such as the full range of emission line fluxes relative to the continuum. The only form of intrinsic dust reddening comes from what is already present in the five basis SEDs via the training set used to create the basis templates, and linear combinations thereof do not span the full range of realistic dust extinction observed in galaxy populations.

While these idealized conditions limit the realism of our mock data, they are irrelevant to the controlled experimental conditions of this study, if anything assuring that differentiation in the performance of the photo- z PDF codes is due to the inferential techniques rather than nuances in the data.

2.2 LSST-like mock observations

Given the SED, absolute r -band magnitude, and true redshift of each simulated galaxy, we computed apparent magnitudes in the six LSST filter passbands, $ugrizy$. We assigned magnitude errors in the six bands using the simple model of Ivezić et al. (2008), assuming achievement of the full 10-year depth, with a modification of fiducial LSST total numbers of 30-second visits for photometric error generation: we assume 60 visits in u -band, 80 visits in g -band, 180 visits in r -band, 180 visits in i -band, 160 visits in z -band, and 160 visits in y -band.

As a consequence of adding Gaussian-distributed photometric errors, 2.0% of our galaxies exhibit a negative flux in one or more bands, the vast majority of which are in the u -band. We deem such negative fluxes *non-detections* and assign a placeholder magnitude of 99.0 in the catalogue to indicate to the photo- z PDF codes that such galaxies would be “looked at but not seen” in multi-band forced photometry.

The full dataset thus covers 400 square degrees and contains 238 million galaxies of redshift $0 < z \leq 8.7$ down to $r = 29$. Systematic inconsistencies with galaxy colors at $z > 2$ were observed, so the catalogue was limited to $0 < z \leq 2.0$. To obtain a catalogue matching the LSST Gold Sample, we imposed an cut of $i < 25.3$, which gives a signal-to-noise ratio $\gtrsim 30$ for most galaxies. In order for statistical errors to be subdominant to the systematic errors we aim to probe, we further reduced the sample size to $< 10^7$ galaxies by isolating ~ 16.8 square degrees selected from five separate spatial regions of the simulation. We refer to this final set of galaxies as DC1, for the first LSST-DESC Data Challenge.

2.3 Shared prior information

For the purpose of performing a controlled experiment that compares photo- z PDF codes on equal footing as a baseline for a future sensitivity analysis, we take care to provide each with maximally optimistic prior information. Redshift estimation approaches built upon physical modeling and machine learning alike have a notion of prior information considered beyond the photometry of the data for which redshift is to be constrained: that information is derived from a template library for a model-based code and a training set for a data-driven code. In this initial study, we seek to set a baseline for a later comparison of the performance of photo- z PDF codes under incomplete and non-representative prior

³ <https://github.com/vipasu/addsed>

⁴ <http://kcorrect.org>

4 LSST Dark Energy Science Collaboration

information that will propagate differently in the space of data-driven and model-based algorithms. However, for the baseline case of perfect prior information, physical modeling and machine learning codes can indeed be put on truly equal footing. We outline the equivalent ways of providing all codes perfect prior information below.

2.3.1 Training and test set division

Following the findings of Bernstein & Huterer (2010), Masters et al. (2017) that only 10^4 spectra are necessary to calibrate photo-zs to Stage IV requirements, we aimed to set aside a randomly selected training set of $3 - 5 \times 10^4$ galaxies, $\sim 10\%$ of the full sample. After all cuts described above, we designated the *DC1 training set* of 44 404 galaxies for which observed photometry, true SEDs, and true redshifts would be provided to all codes and the blinded *DC1 test set* of 399 356 galaxies for which photometry alone would be provided to all codes and photo-z PDFs would be requested. The exact form of LSST photometric filter transmission curves were also considered public information that could be used by any code.

2.3.2 Template library construction

We aimed to provide template-fitting codes with complete yet manageable library of templates spanning the space of SEDs of the DC1 galaxies. We constructed $K = 100$ representative templates from the $\sim 5 \times 10^5$ SEDs of the SDSS DR6 NYU-VAGC by using the five-dimensional vectors of SED weight coefficients described above. After regularizing the SED weight coefficients $\in [0, 1]$, we ran a simple K-means clustering algorithm on the five-dimensional space of regularized SED weight coefficients of the SDSS galaxy sample. The resulting clusters were used to define Voronoi cells in the space of weight coefficients, with centre positions corresponding to weights for the k-correct SED components, yielding the 100 SEDs that comprise the *DC1 template set* provided to all template-based codes. We did not, however, exclude from consideration template-based codes that made modifications in their use of these templates due to architecture limitations (as opposed to knowledge of the experimental conditions that could artificially boost the code's apparent performance), with deviations noted in Section 3.

3 METHODS

Here we summarize the twelve photo-z PDF codes compared in this study, also in Table 1, which include both established and emerging approaches in template fitting and machine learning. Though not exhaustive, this sample represents codes for which there was sufficient expertise within the LSST-DESC Photometric Redshifts Working Group. Some aspects of data treatment were left to the individual code runners, for example, whether/how to split the available data with known redshifts into separate training and validation sets.

Another key difference is the treatment of non-detections in one or more bands: some codes ignore incomplete bands, while others replace the value with either an estimate for the detection limit, the mean of other values in

the training set, or another default value. There are varying conventions among machine learning based codes for treatment of non-detections, and no one prescription dominates in the photo-z literature. The specific choices for each code affect the results and contribute to the implicit prior influencing their output. However, we remind the reader that only 2.0 per cent of our sample has non-detections, almost exclusively in the *u*-band, and thus should not dominate the code performance differences. The authors welcome interest from those outside LSST-DESC to have their codes assessed in future investigations that build upon this one.

We describe the algorithms and implementations of the model-based and data-driven codes in Sections 3.1 and 3.2 respectively, with a straw-person approach included in Section 3.3.

3.1 Template-based Approaches

We test three publicly available and commonly used template-based codes that share the standard physically motivated approach of calculating model fluxes for a set of template SEDs on a grid of redshift values and evaluating a χ^2 merit function using the observed and model fluxes:

$$\chi^2(z, T, A) = \sum_i^{N_{\text{filt}}} \left(\frac{F_{\text{obs}}^i - A F_{\text{pred}}^i(T, z)}{\sigma_{\text{obs}}^i} \right)^2 \quad (1)$$

where A is a normalization factor, $F_{\text{pred}}^i(T, z)$ is the flux predicted for a template T at redshift z , F_{obs}^i is the observed flux in a given band i , σ_{obs}^i is the observed flux error, and N_{filt} is the total number of filters, in our case the six *ugrizy* LSST filters. The likelihood is a sum of observed flux error σ_{obs}^i -weighted squared differences between the observed flux F_b^{obs} and the normalized predicted flux $F_b^{\text{mod}}(T, z)$ in N_{filt} photometric filters b , which is the LSST *ugrizy* filters in this case. Specific implementation details of each code, e. g. prior form and implementation, are described below.

3.1.1 BPZ

Bayesian Photometric Redshift (BPZ⁵, Benítez 2000) determines the likelihood $p(C|z, T)$ of a galaxy's observed colours C for a set of SED templates T at redshifts z . The BPZ likelihood is related to the χ^2 likelihood by $p(C|z, T) \propto \exp[-\chi^2/2]$. Given a Bayesian prior $p(z, T|m_0)$ over apparent magnitude m_0 and type T , and assuming that the SED templates are spanning and exclusive, BPZ constructs the redshift posterior $p(z|C, m_0)$ by marginalizing over all SED templates with the form $p(z|C, m_0) \propto \sum_T p(C|z, T) p(z, T|m_0)$ (Eq. 3 from Benítez 2000), corresponding to setting the parameter PROBS_LITE=TRUE in the BPZ parameter file. The BPZ prior is the product of an SED template proportion that varies with apparent magnitude $p(T|m_0)$ and a prior $p(z|T, m_0)$ over the expected redshift as a function of apparent magnitude and SED template. We anticipate BPZ to outperform other template-based approaches due to the prior that both comprehensively accounts for SED type and is calibrated to the training set.

Here we test BPZ-v 1.99.3 (Benítez 2000) with the DC1

⁵ <http://www.stsci.edu/~dcoe/BPZ/>

Table 1. List of photo-z PDF codes featured in this study

Published code	Type	Public source code
LePhare (Arnouts et al. 1999)	template fitting	http://www.cfht.hawaii.edu/~arnouts/lephare.html
BPZ (Benítez 2000)	template fitting	http://www.stsci.edu/~dcoe/BPZ/
EAZY (Brammer et al. 2008)	template fitting	https://github.com/gbrammer/eazy-photoz
ANNz2 (Sadeh et al. 2016)	machine learning	https://github.com/IftachSadeh/ANNZ
FlexZBoost (Izbicki & Lee 2017)	machine learning	https://github.com/tospis/i/flexcode ; https://github.com/rizbicki/FlexCoDE
GPz (Almosallam et al. 2016b)	machine learning	https://github.com/OxfordML/GPz
METAPhR (Cavuoti et al. 2017)	machine learning	http://dame.dsfs.unina.it
CMNN (Graham et al. 2018)	machine learning	N/A
SkyNet (Graff et al. 2014)	machine learning	http://ccforge.cse.rl.ac.uk/gf/project/skynet/
TPZ (Carrasco Kind & Brunner 2013)	machine learning	https://github.com/mgckind/MLZ
Delight (Leistedt & Hogg 2017)	hybrid	https://github.com/ixkael/Delight
trainZ	machine learning	See Section 3.3

330 template set of Section 2.3.2. To keep the number of free pa-
 331 rameters manageable, the DC1 template set is pre-sorted by
 332 the rest-frame $u - g$ colour and split into three broad classes
 333 of SED template, equivalent to the E, Sp and Im/SB types.
 334 The Bayesian prior term $p(T|m_0)$ was derived directly from
 335 the DC1 training set, and the other term $p(z|T, m_0)$ was
 336 chosen to be the best fit for the eleven free parameters from
 337 the functional form of Benítez (2000). We use template in-
 338 terpolation, creating two linearly interpolated templates be-
 339 tween each basis SED (sorted by rest-frame $u - g$ colour) by
 340 setting the parameter `INTERP=2`. Prior to running the code,
 341 the non-detection placeholder magnitude was replaced with
 342 an estimate of the one- σ detection limit for the undetected
 343 band as a proxy for a value close to the estimated sky noise
 344 threshold.

3.1.2 EAZY

345 Easy and Accurate Photometric Redshifts from Yale (EAZY⁶,
 346 Brammer et al. 2008) extends the basic χ^2 fit procedure that
 347 defines template-fitting approaches. The algorithm models
 348 the observed photometry with a linear combination of tem-
 349 plate SEDs at each redshift. The best-fit SED at each red-
 350 shift is found by simultaneously fitting one, two, or all of
 351 the templates via χ^2 minimization, which is distinct from
 352 marginalizing across all templates. The minimized χ^2 like-
 353 lihood at each redshift is then combined with an apparent
 354 magnitude prior to obtain the redshift posterior PDF. We
 355 note that the utilization of the best-fit SED conditioned on
 356 redshift rather than a proper marginalization does not lead
 357 to the correct posterior distribution, an implementation is-
 358 sue that has now been identified and will be addressed by
 359 the developers in the future.

360 In contrast with BPZ, EAZY’s apparent magnitude prior is
 361 independent of SED, though it was derived empirically from
 362 the DC1 training set. The EAZY architecture cannot accept
 363 a template set other than the same five basis templates em-
 364 ployed by `k-correct` when constructing the DC1 catalogue,
 365 but, for consistency with the experimental scope of perfect
 366 prior information, EAZY’s flexible `all-templates` mode was
 367 used to fit the photometric data with a linear combination
 368 of the five basis templates. Though EAZY can account for
 369 uncertainty in the template set by adding in quadrature to
 370 the flux errors an empirically derived template error as a

372 function of redshift, we set the template error to zero since
 373 the same templates were in fact used to produce the DC1
 374 photometry.

3.1.3 LePhare

375 Photometric Analysis for Redshift Estimate (LePhare⁷,
 376 Arnouts et al. 1999; Ilbert et al. 2006) uses the χ^2 of Equa-
 377 tion 1 to match observed colors with those predicted from a
 378 template set. The template set can be semi-empirical or en-
 379 tirely synthetic. The reported photo-z PDF is an arbitrary
 380 normalization of the likelihood evaluated on the output red-
 381 shift grid.

382 Here we use LePhare-v 2.2 with the DC1 template set
 383 of Section 2.3.2. Unlike both BPZ and EAZY, LePhare uses
 384 generic, SED-independent priors that are not tuned to the
 385 DC1 data set.

3.2 Machine Learning-based Approaches

387 We compared nine data-driven photo-z estimation ap-
 388 proaches, eight of which are described in this section and one
 389 of which is discussed in Section 3.3. Because the algorithms
 390 differ more from one another and the techniques are rela-
 391 tive newcomers to the astronomical literature, we provide
 392 somewhat more detail about the implementations below.

3.2.1 ANNz2

395 ANNz2⁸ (Sadeh et al. 2016) supports several machine learn-
 396 ing algorithms, including artificial neural networks (ANN),
 397 boosted decision tree, and k-nearest neighbour (KNN) re-
 398 gression. In addition to accounting for errors on the input
 399 photometry, ANNz2 uses the KNN-uncertainty estimate of
 400 Oyaizu et al. (2008) to quantify uncertainty in the choice of
 401 method over multiple runs. Using the Toolkit for Multivariate
 402 Data Analysis with ROOT⁹, ANNz2 can return the results
 403 of running a single machine learning algorithm, a “best”
 404 choice of the results from simultaneously running multiple
 405 algorithms (based on evaluation the cumulative distribution
 406 functions of validation set objects), or a combination of the

⁷ <http://www.cfht.hawaii.edu/~arnouts/lephare.html>

⁸ <https://github.com/IftachSadeh/ANNZ>

⁹ <http://tmva.sourceforge.net/>

⁶ <https://github.com/gbrammer/eazy-photoz>

6 LSST Dark Energy Science Collaboration

407 results of multiple algorithms weighted by their method uncertainties averaged over multiple runs.

409 In this study, we used ANNz2-v.2.0.4 to output only the
410 result of the ANN algorithm. Photo-z PDFs were produced
411 by running an ensemble of 5 ANNs with a 6 : 12 : 12 : 1
412 architecture corresponding to the 6 *ugrizy* inputs, 2 hidden
413 layers with 12 nodes each, and 1 output of redshift. Each of
414 the five ANNs was trained with different random seeds for
415 the initialization of input parameters, reserving half of the
416 training set for validation to prevent overfitting. Undetected
417 galaxies were excluded from the training set, and per-band
418 non-detections in the test set were replaced with the mean
419 magnitude in that band within the entire test set.

465 ance $\sigma_{\text{train}}^2(\text{PPF}_{20}/0.95)^2 - 1$ to account for the correspond-
466 ing growth of the effective PPF to include 20 neighbors.

467 3.2.3 Delight

468 **Delight**¹⁰ (Leistedt & Hogg 2017) is a hybrid technique that
469 infers photo-zs with a data-driven model of latent SEDs and
470 a physical model of photometric fluxes as a function of red-
471 shift. Generally, machine learning methods rely on represen-
472 tative training data with shared photometric filters, while
473 template based methods rely on a complete library of tem-
474 plates based on physical models constructed. **Delight** aims
475 to take the best aspects of both approaches by construct-
476 ing a large collection of latent SED templates (or physical
477 flux-redshift models) from training data, with a template
478 SED library as a guide to the learning of the model, thereby
479 circumventing the machine learning prerequisite of represen-
480 tative training data in the same photometric bands and the
481 template fitting requirement of detailed galaxy SED models.
482 It models noisy observed flux $\hat{\mathbf{F}} = \mathbf{F} + F_b$ as a sum of a noise-
483 less flux plus a Gaussian processes $F_b \sim \mathcal{GP}(\mu^F, k^F)$ with
484 zero mean function μ^F and a physically motivated kernel k^F
485 that induces realistic correlations in flux-redshift space.

486 From a template-fitting perspective, each test set galaxy
487 has a posterior $p(z|\hat{\mathbf{F}}) \approx \sum_i p(\hat{\mathbf{F}}|z, T_i)p(z|T_i)p(T_i)$ of red-
488 shift z conditioned on noisy flux $\hat{\mathbf{F}}$, where $p(z|T_i)p(T_i)$ cap-
489 tures prior information about the redshift distributions and
490 abundances of the galaxy templates T_i . As in traditional
491 template fitting, each likelihood $p(\hat{\mathbf{F}}|\mathbf{F})$ relates the noisy flux
492 $\hat{\mathbf{F}}$ with the noiseless flux \mathbf{F} predicted by the model of a linear
493 combination of templates, carefully constructed to account
494 for model uncertainties and different normalization of the
495 same SED, plus the Gaussian process term.

496 The machine learning approach appears in the inclu-
497 sion of a pairwise comparison term $p(\mathbf{F}|z, z_j, \hat{\mathbf{F}}_j)$ for the
498 prediction of model flux \mathbf{F} at a model redshift z with re-
499 spect to training set galaxy j with redshift z_j and ob-
500 served flux $\hat{\mathbf{F}}_j$. Thus the photo-z posterior $p(\hat{\mathbf{F}}|z, T_i) =$
501 $\int p(\hat{\mathbf{F}}|\mathbf{F})p(\mathbf{F}|z, z_j, \hat{\mathbf{F}}_j)d\mathbf{F}$ may be interpreted as the proba-
502 bility that the training and the target galaxies have the same
503 SED at different redshifts. The flux prediction $p(\mathbf{F}|z, z_j, \hat{\mathbf{F}}_j)$
504 of the training galaxy at redshift z is modeled via the Gaus-
505 sian process described above; more detail is provided in
506 Leistedt & Hogg (2017).

507 In this study, the default settings of **Delight** were used,
508 with the exception that the PDF bins were set to be linearly-
509 spaced rather than logarithmic. The Gaussian process was
510 trained using the full DC1 training set. We used the full DC1
511 template set with a flat prior in magnitude and SED type.
512 Photometric uncertainties from the inputs are propagated
513 into the code, while non-detections for each band are set to
514 the mean of the respective bands.

515 3.2.4 FlexZBoost

516 **FlexZBoost**¹¹ (Izbicki & Lee 2017) is built on **FlexCode**, a
517 general-purpose methodology for converting any conditional

10 <https://github.com/ixkael/Delight>

11 <https://github.com/tpospisi/flexcode>;
<https://github.com/rizbicki/FlexCoDE>

mean point estimator of z to a conditional density estimator $p(z|\mathbf{x}) \equiv f(z|\mathbf{x})$, where \mathbf{x} here represents our photometric covariates and errors. **FlexZBoost** expands the unknown function $f(z|\mathbf{x}) = \sum_i \beta_i(\mathbf{x})\phi_i(z)$ using an orthonormal basis $\{\phi_i(z)\}_i$. By the orthogonality property, the expansion coefficients $\beta_i(\mathbf{x}) = \mathbb{E}[\phi_i(z)|\mathbf{x}] \equiv \int f(z|\mathbf{x})\phi_i(z)dz$ are thus conditional means. The expectation value $\mathbb{E}[\phi_i(z)|\mathbf{x}]$ of the expansion coefficients conditioned on the data is equivalent to the regression of the space of possible redshifts on the space of possible photometry. Thus the expansion coefficients $\beta_i(\mathbf{x})$ can be estimated from the data via regression to yield the conditional density estimate $\hat{f}(z|\mathbf{x})$.

In this paper, we used **xgboost** (Chen & Guestrin 2016) for the regression; it should, however, be noted that **FlexCode-RF**¹¹, based on Random Forests, generally performs better on smaller datasets. As our basis $\phi_i(z)$, we choose a standard Fourier basis. The two tuning parameters in our photo- z PDF estimate are the number I of terms in the series expansion and an exponent α that we use to sharpen the computed density estimates $\hat{f}(z|\mathbf{x}) \propto \hat{f}(z|\mathbf{x})^\alpha$. Both I and α were chosen in an automated way by minimizing the weighted L_2 -loss function (Eq. 5 in Izbicki & Lee 2017) on a validation set comprised of a randomly selected 15% of the DC1 training set. While **FlexCode**'s lossless native encoding stores each photo- z PDF using the basis coefficients $\beta_i(\mathbf{x})$, we discretized the final estimates into 200 linearly-spaced redshift bins $0 < z < 2$ to match the consistent output format of the experimental conditions.

546 3.2.5 GP_z

547 GP_z¹² (Almosallam et al. 2016a,b) is a sparse Gaussian process based code, a scalable approximation of full Gaussian Processes (Rasmussen & Williams 2006), that produces input-dependent variance estimates corresponding to 551 heteroscedastic noise. The model assumes a Gaussian posterior probability $p(z|\mathbf{x}) = \mathcal{N}(z|\mu(\mathbf{x}), \sigma(\mathbf{x})^2)$ of the output redshift z given the input photometry \mathbf{x} . The mean $\mu(\mathbf{x})$ and the variance $\sigma(\mathbf{x})^2$ are modeled as functions $f(\mathbf{x}) = \sum_{i=1}^m w_i \phi_i(\mathbf{x})$ linear combinations of m basis functions $\{\phi_i(\mathbf{x})\}_{i=1}^m$ with associated weights $\{w_i\}_{i=1}^m$. The details on how to learn the parameters of the model and the hyper-parameters of the basis functions are described in Almosallam et al. (2016b). GP_z's variance estimate is composed of a model uncertainty term corresponding to sparsity of the training set photometry and a noise uncertainty term encompassing noisy photometric observations, enabling quantification of any need for more representative or more precise training samples. GP_z may also weight training set samples by importance according to $|z_{\text{spec}} - z_{\text{phot}}|/(1+z_{\text{spec}})$ to minimize the normalized photo- z point estimate error, however, this function may be adapted to photo- z PDFs, pressuring the model to dedicate more resources to test set galaxies that are not well-represented in the training set.

To smooth the long tail in the distribution of magnitude errors, we use the log of the magnitude errors, improving numerical stability and eliminating the need for constraints on the optimization process. Unobserved magnitudes $x_u = \mu_u + \Sigma_{uo}\Sigma_{oo}^{-1}(x_o - \mu_o)$ were imputed from

575 observed magnitudes x_o and the training set mean μ and 576 covariance Σ using a linear model. This is the optimal 577 expected value of the unobserved variables given the observed 578 ones under the assumption that the distribution is jointly 579 Gaussian; note that this reduces to a simple average if the 580 covariates are independent with $\Sigma_{uo} = 0$. We reserved for 581 validation 20% of the training set and used the Variable 582 Covariance option in GP_z with 200 basis functions (see Al- 583 mosallam et al. (2016b) for details), neglecting to apply cost- 584 sensitive learning options.

585 3.2.6 METAPhōR

586 Machine-learning Estimation Tool for Accurate Photometric 587 Redshifts (METAPhōR¹³, Cavuoti et al. 2017) is based on 588 the Multi Layer Perceptron with Quasi Newton Algorithm 589 (MLPQNA) with the least square error model and Tikhonov 590 L_2 -norm regularization (Hofmann & Mathé 2018). Photo- z 591 PDFs are generated by running N trainings on the same 592 training set, or M trainings on M different random samplings 593 of the training set. Upon regression of the test set, the 594 photometry m_{ij} of each test set galaxy j in filter i is 595 perturbed according to $m'_{ij} = m_{ij} + \alpha_i F_{ij} \epsilon$ in terms of 596 the standard normal random variable $\epsilon \sim \mathcal{N}(0, 1)$, a multi- 597 multiplicative constant α_i permitting accommodation of multi- 598 survey photometry, and a bimodal function F_{ij} composed of 599 a polynomial fit of the mean magnitude errors on the binned 600 bands plus a constant term representing the threshold below 601 which the polynomial's noise contribution is negligible 602 (Brescia et al. 2018).

603 In this work, we used a hierarchical KNN to replace 604 non-detections with values based on their neighbors. The 605 usual cross-validation of redshift estimates and PDFs was 606 also omitted for this study.

607 3.2.7 SkyNet

608 SkyNet¹⁴ (Graff et al. 2014) employs a neural network based 609 on a second order conjugate gradient optimization scheme 610 (see Graff et al. 2014, for further details). The neural net- 611 work is configured as a standard multilayer perceptron with 612 three hidden layers and one input layer with 12 nodes cor- 613 responding to the 6 photometric magnitudes and their mea- 614 surement errors.

615 SkyNet's classifier mode uses a cross-entropy error func- 616 tion with a 20:40:40 node (all rectified linear units) architec- 617 ture for each hidden layer and an output layer of 200 nodes 618 corresponding to 200 bins for the PDF, with a softmax acti- 619 vation function to enforce the normalization condition that 620 the probabilities sum to unity. While previous implemen- 621 tations of the code (see Appendix C.3 of Sánchez et al. 2014; 622 Bonnett 2015) implement a sliding bin smoothing, no such 623 procedure was used in this study.

624 We pre-whitened the data by pegging the magnitudes 625 to (45,45,40,35,42,42) and errors to (20,20,10,5,15,15) for 626 ugrizy filters, respectively. To avoid over-fitting, 30% of the 627 training set was reserved for validation, and training was 628 halted as soon as the error rate began to increase on the

¹² <https://github.com/OxfordML/GPz>

¹³ <http://dame.dsfa.unina.it>

¹⁴ <http://ccpforge.cse.rl.ac.uk/gf/project/skynet/>

8 LSST Dark Energy Science Collaboration

validation set. The weights were randomly initialized based on normal sampling.

3.2.8 TPZ

Trees for Photo- z (TPZ¹⁵, Carrasco Kind & Brunner 2013; Carrasco Kind & Brunner 2014) uses prediction trees and random forest techniques to estimate photo- z PDFs. TPZ recursively splits the training set into branch pairs based on maximizing information gain among a random subsample of features, to minimize correlation between the trees, terminating only when a newly created leaf meets a criterion, such as a leaf size minimum or a variance threshold. The regions in each terminal leaf node correspond to a subsample of the training set with similar properties. Bootstrap samples from the training set photometry and errors are used to build a set of prediction trees.

To run TPZ, we replaced non-detections with an approximation of the 1σ detection threshold based on the error forecast of the 10-year LSST data, i. e. $dm = 2.5 \log(1 + N/S)$ where $dm \sim 0.7526$ magnitudes for $N/S = 1$. We calibrated TPZ with the Out-of-Bag cross-validation technique (Breiman et al. 1984; Carrasco Kind & Brunner 2013) to evaluate its predictive validity and determine the relative importance of the different input attributes. We grew 100 trees to a minimum leaf size of 5 using the *ugri* magnitudes, all $u - g, g - r, r - i, i - z, z - y$ colours, and the associated errors, as the z and y magnitudes did not show significant correlation with the redshift in our cross-validation. We partitioned our redshift space into 200 bins and smoothed each individual PDF with a smoothing scale of twice the bin size.

3.3 trainZ: a pathological photo- z PDF estimator

We also consider a pathological photo- z PDF estimation method, dubbed **trainZ**, which assigns each test set galaxy a photo- z PDF equal to the normalized redshift distribution $N(z)$ of the training set, according to

$$p(z|\{z_j\}) \equiv \frac{1}{N_{\text{train}}} \sum_{i=1}^{N_{\text{train}}} \begin{cases} 1 & \text{if } z_k \leq z_i < z_{k+1} \\ 0 & \text{otherwise} \end{cases}. \quad (2)$$

Unlike the other methods, the **trainZ** estimator is *independent of the photometric data*, effectively performing a KNN procedure with $k = N_{\text{train}}$.

Though **trainZ** is strongly vulnerable to a nonrepresentative training set, it should optimize performance metrics probing the ensemble properties of the galaxy sample, modulo Poisson error due to small sample size, as the training set and test set are drawn from the same underlying population. We will demonstrate its performance under the metrics of Section 4 and discuss it as an illustrative experimental control case in Section 6.1 to highlight the limitations of our evaluation criteria for photo- z PDFs.

4 ANALYSIS

The goal of this study is to evaluate the degree to which photo- z PDFs of each method can be trusted for a generic

analysis. The overloaded “ $p(z)$ ” is a widespread abuse of notation that obfuscates this goal, so we dedicate attention to dismantling it here. Galaxies have redshifts z and photometric data d drawn from a joint probability space $p(z, d)$ in nature. As a result, each observed galaxy i has a *true posterior photo- z PDF* $p(z|d_i)$ as well as a true likelihood $p(d|z_i)$. There are a number of metrics that can be used to test the accuracy of a photo- z posterior as an estimator of a true photo- z posterior if the true photo- z PDF is known. However, the true photo- z PDF is in general not accessible unless the photometry is in fact drawn from a ground truth for the joint probability density of redshift and photometry $p(z, d)$. In contrast, existing mock catalogs produce redshift-photometry pairs (z, d) by a deterministic algorithm that does not correspond to a joint probability density from which one can take samples. In these cases there is no “true PDF” for an individual object, and most measures of PDF fidelity will necessarily be restricted to probing the quality of the ensemble of photo- z PDFs. (See §6.2 for a discussion of how one might circumvent this limitation.)

Before describing the metrics appropriate to the DC1 data set, we outline the philosophy behind our choices. A photo- z PDF estimator derived by method H must be understood as a posterior probability distribution

$$\hat{p}_i^H(z) \equiv p(z|d_i, I_D, I_H), \quad (3)$$

conditioned not only on the photometric data d_i for that galaxy but also on parameters encompassing a number of things that will differ depending on the method H used to produce it, namely the often implicit assumptions I_H necessary for the method to be valid and any inputs I_D it takes as prior information, such as a template library or training set. Because of this, direct comparison of photo- z PDFs produced by different methods is in some sense impossible; even if they share the same external prior information I_D , by definition they cannot be conditioned on the same assumptions I_H , otherwise they would not be distinct methods at all. We call I_H the *implicit prior* specific to the method, though some aspects of its nature may be discerned.

In this study, we isolate the effect of differences in prior information I_H specific to each method by using a single training set I_D^{ML} for all machine learning-based codes and a single template library I_D^{T} for all template-based codes. These sets of prior information are carefully constructed to be representative and complete, so we have $I_D \equiv I_D^{\text{ML}} \equiv I_D^{\text{T}}$ for every method H . Under this assumption, a ratio of posteriors of codes is in effect a ratio of the implicit posteriors $p(z|d_i, I_H')$ since the external prior information I_D is present in the numerator and denominator. Thus comparisons of $\hat{p}_i^H(z)$ isolate the effect of the method used to obtain the estimator, which should enable interpretation of the differences between estimated PDFs in terms of the specifics of the method implementations.

The exact implementation of the metrics theoretically depends on the parametrization of the photo- z PDFs, which may differ across codes and can affect the precision of the estimator (Malz et al. 2018). Even considering a single method under the same parametrization, such as the 200-bin $0 < z < 2$ piecewise constant function used here, the exact bin definitions must affect the result. The piecewise constant format is chosen because of its established presence in the literature, and the choice of 200 bins was motivated by the

¹⁵ <https://github.com/mgckind/MLZ>

approximate number of columns expected to be available for storage of photo- z PDFs for the final LSST Project tables.¹⁶ We will discuss the choice of photo- z PDF parameterization further in Section 6.

This analysis is conducted using the `qp`¹⁷ software package (Malz & Marshall 2018) for manipulating and calculating metrics of univariate PDFs. We present the metrics of photo- z PDFs that address our goals in the sections below. Section 4.1 outlines aggregate metrics of a catalogue of photo- z PDFs, and Section 4.2 presents a metric of individual photo- z PDFs in the absence of true photo- z PDFs. Though the outmoded practices should not be encouraged, those seeking a connection to previous comparison studies will find metrics of redshift point estimate reductions of photo- z PDFs in Appendix B and metrics of a science-specific summary statistics heuristically derived from photo- z PDFs in Appendix A.

4.1 Metrics of photo- z PDF ensembles

Because LSST’s photo- z PDFs will be used for many scientific applications, some of which require accuracy of each individual catalog entry, we consider several metrics that probe the population-level performance of the photo- z PDFs. As we have the true redshifts but not true photo- z PDFs for comparison, we remind the reader of the Cumulative Distribution Function (CDF)

$$\text{CDF}[f, q] \equiv \int_{-\infty}^q f(z) dz, \quad (4)$$

of a generic univariate PDF $f(z)$, which is used as the basis for several of our metrics. We describe metrics based on the CDF in Section 4.1.1 and metrics of summary statistics thereof in Section 4.1.2.

4.1.1 CDF-based metrics

A quantile of a distribution is the value q at which the CDF of the distribution is equal to Q ; percentiles and quartiles are familiar examples of linearly spaced sets of 100 and 4 quantiles, respectively. The quantile-quantile (QQ) plot serves as a graphical visualization for comparing two distributions, where the quantiles of one distribution are plotted against the quantiles of the other distribution, providing an intuitive way to qualitatively assess the consistency between an estimated distribution and a true distribution. The closer the QQ plot is to diagonal, the closer the match between the distributions.

The probability integral transform (PIT)

$$\text{PIT} \equiv \text{CDF}[\hat{p}, z_{\text{true}}] \quad (5)$$

is the CDF of a photo- z PDF evaluated at its true redshift, and the distribution of PIT values probes the average accuracy of the photo- z PDFs of an ensemble of galaxies. The distribution of PIT values is effectively the derivative of the QQ plot. A catalogue of accurate photo- z PDFs should have a PIT distribution that is uniform $U(0, 1)$, and deviations

¹⁶ See, e. g. the LSST Data Products Definition Document, available at: <https://ls.st/dpdd>

¹⁷ <http://github.com/aimalz/qp/>

from flatness are interpretable: overly broad photo- z PDFs induce underrepresentation of the lowest and highest PIT values, whereas overly narrow photo- z PDFs induce overrepresentation of the lowest and highest PIT values. Catastrophic outliers with a true redshift outside the support of its photo- z PDF have $\text{PIT} \approx 0$ or $\text{PIT} \approx 1$.

The PIT distribution has been used to quantify the performance of photo- z PDF methods in the past (e. g. Borodoloi et al. 2010; Polsterer et al. 2016; Tanaka et al. 2018). Tanaka et al. (2018) use the histogram of PIT values as a diagnostic indicator of overall code performance, while Freeman et al. (2017) independently define the PIT and demonstrate how its individual values may be used both to perform hypothesis testing (via, e. g. the KS, CvM, and AD tests; see below) and to construct quantile-quantile plots. Following Kodra & Newman (in prep.) we define the PIT-based catastrophic outlier rate as the fraction of galaxies with $\text{PIT} < 0.0001$ or $\text{PIT} > 0.9999$, which should total 0.0002 for an ideal uniform distribution.

4.1.2 Summary statistics of CDF-based metrics

We evaluate a number of quantitative metrics derived from the visually interpretable QQ plot and PIT histogram, built on the Kolmogorov-Smirnov (KS) statistic

$$\text{KS} \equiv \max_z \left(\left| \text{CDF}[\hat{f}, z] - \text{CDF}[\tilde{f}, z] \right| \right), \quad (6)$$

interpretable as the maximum difference between the CDFs of an approximating univariate distribution $\hat{f}(z)$ and a reference distribution $\tilde{f}(z)$, in this case $U(0, 1)$. We also consider two variants of the KS statistic. A cousin of the KS statistic, the Cramer-von Mises (CvM) statistic

$$\text{CvM}^2 \equiv \int_{-\infty}^{+\infty} (\text{CDF}[\hat{f}, z] - \text{CDF}[\tilde{f}, z])^2 d\text{CDF}[\tilde{f}, z] \quad (7)$$

is the mean-squared difference between the CDFs of an approximate and true PDF. The Anderson-Darling (AD) statistic

$$\text{AD}^2 \equiv N_{\text{tot}} \int_{-\infty}^{+\infty} \frac{(\text{CDF}[\hat{f}, z] - \text{CDF}[\tilde{f}, z])^2}{\text{CDF}[\tilde{f}, z](1 - \text{CDF}[\tilde{f}, z])} d\text{CDF}[\tilde{f}, z] \quad (8)$$

is a weighted mean-squared difference featuring enhanced sensitivity to discrepancies in the tails of the distribution. In anticipation of a substantial fraction of galaxies having PIT of 0 or 1, a consequence of catastrophic outliers, we evaluate the AD statistic with modified bounds of integration (0.01, 0.99) to exclude those extremes in the name of numerical stability.

4.2 Conditional Density Estimate (CDE) Loss: a metric of individual photo- z PDFs

The BUZZARD simulation process precludes testing the degree to which samples from our photo- z posteriors reconstruct the space of $p(z, \text{data})$. To the knowledge of the authors, there is only one metric that can be used to evaluate the performance of individual photo- z PDF estimators in the absence of true photo- z posteriors. The conditional density estimation (CDE) loss is an analogue to the familiar root-mean-square-error used in conventional regression, defined

as

$$L(f, \hat{f}) = \int \int (f(z|\mathbf{x}) - \hat{f}(z|\mathbf{x}))^2 dz dP(\mathbf{x}), \quad (9)$$

where $f(z|\mathbf{x})$ is the true photo- z PDF that we do not have and $\hat{f}(z|\mathbf{x})$ is an estimate thereof, in terms of the photometry \mathbf{x} . (See Section 3.2.4 for a review of the notation.) We estimate the CDE loss via

$$\hat{L}(f, \hat{f}) = \mathbb{E}_{\mathbf{x}} \left[\int \hat{f}(z | \mathbf{X})^2 dz \right] - 2\mathbb{E}_{\mathbf{X}, Z} \left[\hat{f}(Z | \mathbf{X}) \right] + K_f, \quad (10)$$

where the first term is the expectation value of the photo- z posterior with respect to the marginal distribution of the photometric covariates \mathbf{X} , the second term is the expectation value with respect to the joint distribution of \mathbf{X} and the space Z of all possible redshifts, and the third term K_f is a constant depending only upon the true conditional densities $f(z|\mathbf{x})$. We may estimate these expectations empirically on the test or validation data (Eq. 7 in Izbicki et al. 2017) without knowledge of the true densities.

5 RESULTS

We begin with a demonstrative visual inspection of the photo- z PDFs produced by each code for individual galaxies. Figure 1 shows the photo- z PDFs for four galaxies chosen as examples of photo- z PDF archetypes: a narrow unimodal PDF, a broad unimodal PDF, a bimodal PDF, and a multimodal PDF. We reiterate that under our idealized experimental conditions, differences between codes are the isolated signature of the implicit prior due to the method by which the photo- z PDFs were derived.

The most striking differences between codes are the small-scale features induced by the interaction between the shared piecewise constant parameterization of 200 bins $0 < z < 2$ of Section 4 and the smoothing conditions or lack thereof in each algorithm. The $dz = 0.01$ redshift resolution is sufficient to capture the broad peaks of faint galaxies' photo- z PDFs with large photometric errors but is too broad to resolve the narrow peaks for bright galaxies' photo- z PDFs with small photometric errors. This observation is consistent with the findings of Malz et al. (2018) that the piecewise constant parameterization underperforms in the presence of small-scale structures.

However, the shared small-scale features of ANNz2, METAPhoR, CMNN, and SkyNet are a result of various weighted sums of the limited number of training set galaxies with colors similar to those of the test set galaxy in question, with behavior closer to classification than regression in the case of ANNz2. The settings used on GPz in this work forced broadening of the single Gaussian to cover the multimodal redshift solutions of the other codes.

5.1 Performance on photo- z PDF ensembles

The histogram of PIT values, QQ plot, and QQ difference plot relative to the ideal diagonal are provided in Figure 2, showcasing the biases and trends in the average accuracy of the photo- z PDFs for each code. The high QQ values (i.e. more high than low PIT values) of BPZ, CMNN, Delight,

Table 2. The catastrophic outlier rate as defined by extreme PIT values. We expect a value of 0.0002 for a proper Uniform distribution. An excess over this small value indicates true redshifts that fall outside the non-zero support of the $p(z)$.

Photo- z Code	fraction $\text{PIT} < 10^{-4}$ or > 0.999
ANNz2	0.0265
BPZ	0.0192
Delight	0.0006
EAZY	0.0154
FlexZBoost	0.0202
GPz	0.0058
LePhare	0.0486
METAPhoR	0.0229
CMNN	0.0034
SkyNet	0.0001
TPZ	0.0130
trainZ	0.0002

EAZY, and GPz indicate photo- z PDFs biased low, and the low QQ values (more low than high PIT values) of SkyNet and TPZ indicate photo- z PDFs biased high. The gray shaded band marks the 2σ variance in PIT values found using the trainZ algorithm with a bootstrap resampling of the training set and a sample size of 30,000 galaxies, representing a very conservative estimate of the representative training sample size, and thus an approximate minimal error significance compared to ideal performance. Deviations in the PIT histograms outside of this range show that significant biases are present for some codes.

The PIT histograms of Delight, CMNN, SkyNet, and TPZ feature an underrepresentation of extreme values, indicative of overly broad photo- z PDFs, while the overrepresentation of extreme values for METAPhoR indicate overly narrow photo- z PDFs. These five codes in particular have a free parameter for bandwidth, which may be responsible for this vulnerability, in spite of the opportunity for fine-tuning with perfect prior information. FlexZBoost's "sharpening" parameter (described in Section 3.2.4) played a key role in diagonalizing the QQ plot, indicating a common avenue for improvement in the approaches that share this type of parameter. On the other hand, the three purely template-based codes, BPZ, EAZY, and LePhare, do not exhibit much systematic broadening or narrowing, which may indicate that complete template coverage effectively defends from these effects.

Close inspection of the extremes at PIT values of 0 and 1 reveal spikes in the first and last bin of the PIT histogram for some codes in Figure 2, corresponding to catastrophic outliers where the true redshift lies outside of the support of the $p(z)$. The catastrophic outlier rates are provided in Table 2. As expected, trainZ achieves precisely the 0.0002 value expected of an ideal PIT distribution. ANNz2, FlexZBoost, LePhare, and METAPhoR have notably high catastrophic outlier rates > 0.02 , exceeding 100 times the ideal PIT rate, meriting further investigation.

Figure 3 highlights the relative values of the KS, CvM, and AD test statistics calculated by comparing the PIT distribution and a uniform distribution $U(0, 1)$. METAPhoR and LePhare perform well under the AD but poorly under the KS and CvM due to their high catastrophic outlier rates. ANNz2 and FlexZBoost are the top scorers under these met-

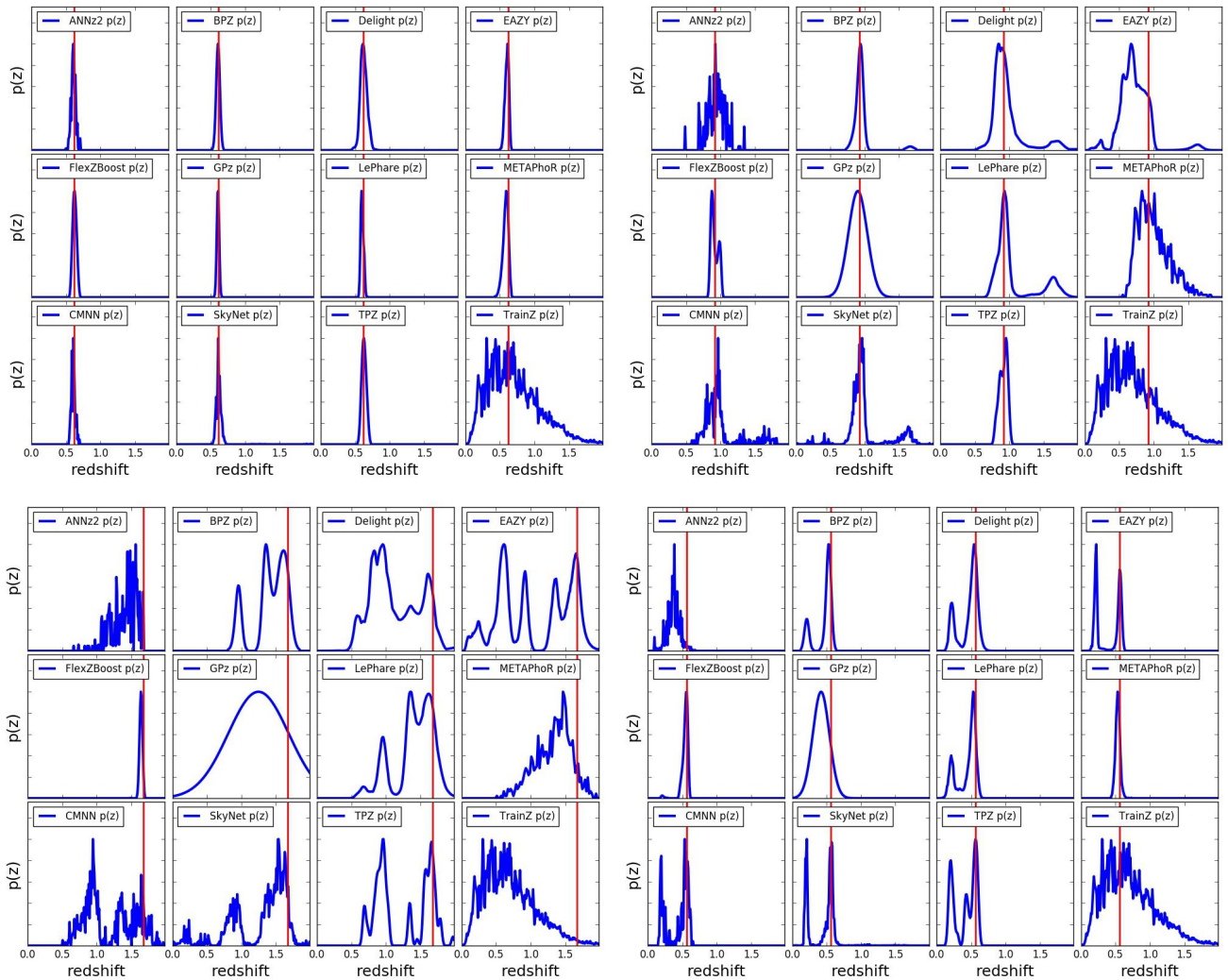


Figure 1. The individual photo- z PDFs (blue) distributions produced by the twelve codes (small panels) on four exemplary galaxies' photometry (large panels) with different true redshifts (red). The photo- z PDFs of all codes share some features for the example galaxies due to physical color degeneracies and photometric errors: tight unimodal $p(z)$ (upper left), broad unimodal $p(z)$ (upper right), bimodal $p(z)$ (lower right), and complex/multimodal $p(z)$ (lower left). The diverse algorithms and implementations induce differences in small-scale structure and sensitivity to physical systematics.

rics of the PIT distribution. ANNz2's strong performance can be attributed to an aspect of the training process in which training set galaxies with a PIT that more closely matches the percentiles of the DC1 training set's redshift distribution are upweighted; in effect, these quantile-based metrics were part of the algorithm itself that may or may not serve it well under more realistic experimental conditions. Similar to what was done for the PIT histograms in Figure 2, we create bootstrap training samples of 30,000 galaxies for use with `trainZ` in order to estimate a conservative statistical floor that we would expect in real data. No code reaches this idealized floor, indicating that all codes suffer some degradation from the ideal when employing their implicit priors, though ANNz2, FlexZBoost, and GPz are within a factor of two.

936 5.2 Performance on individual photo- z PDFs

951 The values of the CDE loss statistic of individual photo- z 952 PDF accuracy are provided in Table 3. It is worth noting 953 that strong performance on the CDE loss, corresponding to 954 lower values of the metric, should imply strong performance 955 on the other metrics, though the inverse is not necessarily 956 true. Thus the CDE loss is the most effective metric for 957 generic science cases.

959 Of the metrics we were able to consider in this experiment, 960 the CDE Loss is the only metric that can appropriately 961 penalize the pathological `trainZ`. Additionally, it favors CMNN 962 and FlexZBoost, the latter of which is optimized for this metric. 963

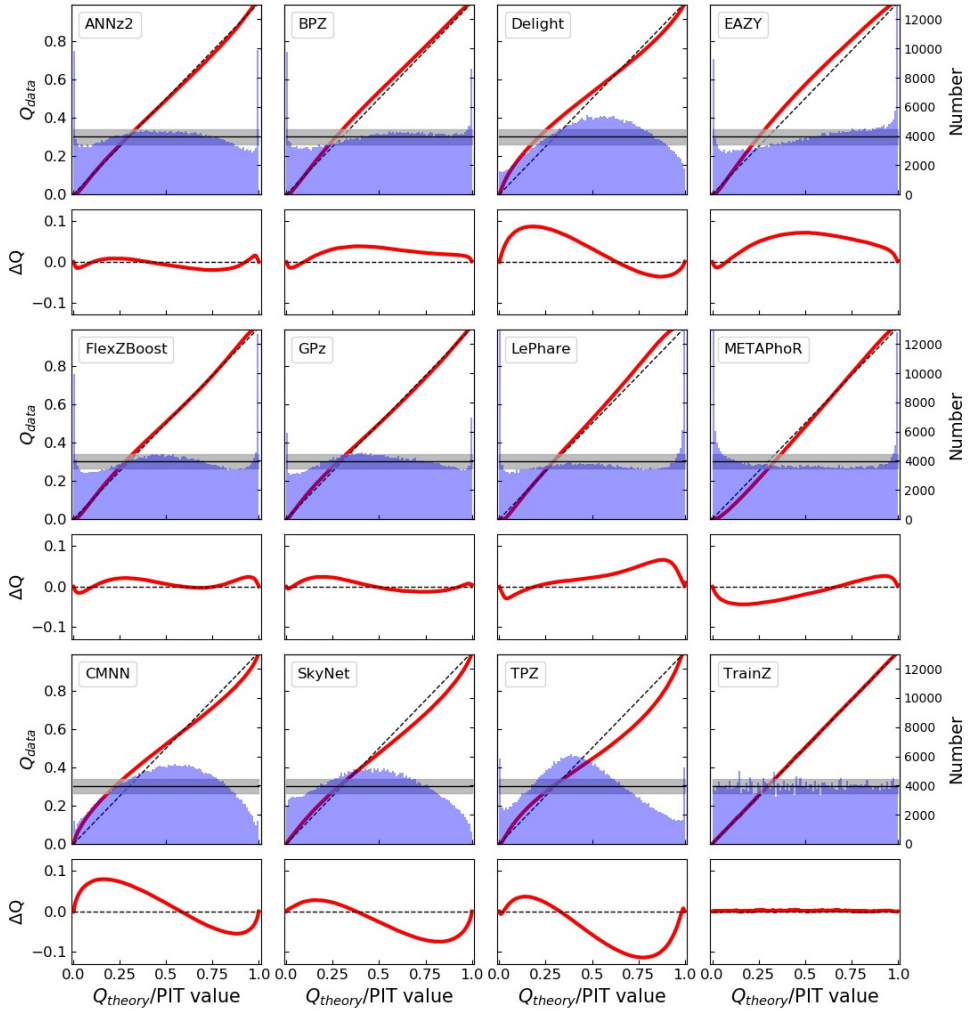


Figure 2. The QQ plot (red) and PIT histogram (blue) of the photo- z PDF codes (panels) along with the ideal QQ (black dashed) and ideal PIT (gray horizontal) curves, as well as a difference plot for the QQ difference from the ideal diagonal (lower inset). The gray shaded region indicates the 2σ range from a bootstrap resampling of the training set with a size of 30,000 galaxies using `trainZ`. The twelve codes exhibit varying degrees of four deviations from perfection: an overabundance of PIT values at the centre of the distribution indicate a catalogue of overly broad photo- z PDFs, an excess of PIT values at the extrema indicates a catalogue of overly narrow photo- z PDFs, catastrophic outliers manifest as overabundances at PIT values of 0 and 1, and asymmetry indicates systematic bias, a form of model misspecification. Values in excess of the 2σ shaded region show that for some codes these errors will be significant given expected training sample sizes.

964 6 DISCUSSION AND FUTURE WORK

965 In contrast with other photo- z PDF comparison papers that
 966 have aimed to identify the “best” code for a given survey, we
 967 have focused on the somewhat more philosophical questions
 968 of how to assess photo- z PDF methods and how to interpret
 969 differences between codes in terms of photo- z PDF per-
 970 formance. In Section 6.1, we reframe the strong performance of
 971 our pathological photo- z PDF technique, `trainZ`, as a cau-
 972 tionary tale about the importance of choosing appropriate
 973 comparison metrics. In Section 6.2, we outline the experi-
 974 ments we intend to build upon this study. In Section 6.3, we
 975 discuss the enhancements of the mock data set that will be
 976 necessary to enable the future experiments.

977 6.1 Interpretation of metrics

978 We remind the reader that contributed codes were given a
 979 goal of obtaining accurate photo- z PDFs, not an accurate
 980 stacked estimator of the redshift distribution, so we do not
 981 expect the same codes to necessarily perform well for both
 982 classes of metrics. Indeed, the codes were optimized for their
 983 interpretation of our request for “accurate photo- z PDFs,”
 984 and we expect that the implementations would have been
 985 adjusted had we requested optimization of the traditional
 986 metrics of Appendices A and B.

987 Furthermore, our metrics are not necessarily able to as-
 988 sess the fidelity of individual photo- z PDFs relative to true
 989 posteriors: in the absence of a “true PDF” from which red-
 990 shifts are drawn, it is difficult to construct metrics to mea-
 991 sure performance for individual galaxies rather than ensem-

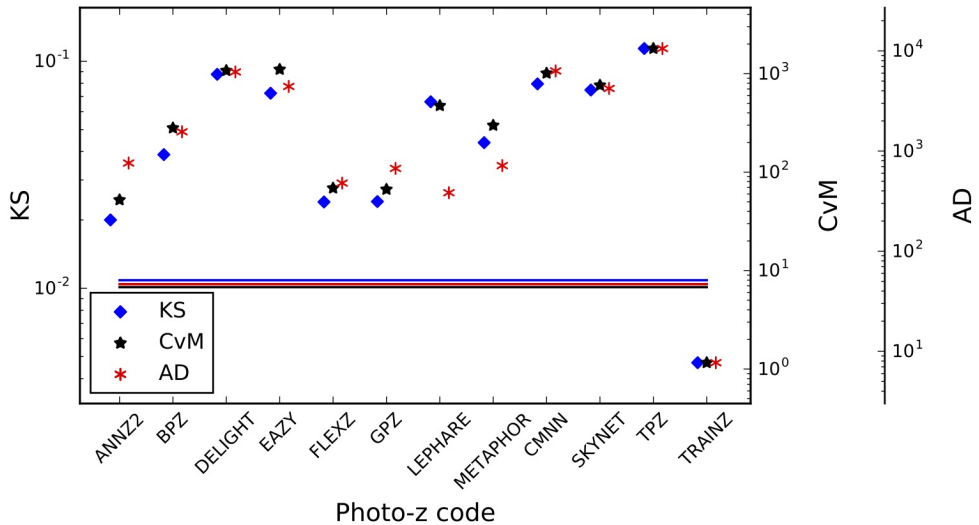


Figure 3. A visualization of the Kolmogorov-Smirnov (KS, blue diamond), Cramer-von Mises (CvM, black star), and Anderson-Darling (AD, red asterisk) statistics for the PIT distributions. There is generally good agreement between these statistics, with differences corresponding to the codes with outstanding catastrophic outlier rates, a reflection in the differences in how each statistic weights the tails of the distribution. Horizontal lines indicate the level of uncertainty found by bootstrapping a training set sample of 30,000 galaxies using `trainZ`; none of the codes reach this conservative ideal floor in expected uncertainty.

Table 3. CDE loss statistic of the individual photo- z PDFs for each code. A lower value of the CDE loss indicates more accurate individual photo- z PDFs, with CMNN and FlexZBoost performing best under this metric.

Photo- z Code	CDE Loss
ANNz2	-6.88
BPZ	-7.82
Delight	-8.33
EAZY	-7.07
FlexZBoost	-10.60
GPz	-9.93
LePhare	-1.66
METAPhOr	-6.28
CMNN	-10.43
SkyNet	-7.89
TPZ	-9.55
<code>trainZ</code>	-0.83

N(z) based statistics. The PIT and other CDF-based metrics upon which modern photo- z PDF comparisons are built (Bordoloi et al. 2010; Polsterer et al. 2016; Tanaka et al. 2018) can be gained by a trivial estimator that yields only an affirmation of prior knowledge uninformed by the data. In other words, such ensemble metrics are not appropriate for the task of selecting photo- z PDF codes for analysis pipelines.

The CDE loss and point estimate metrics appropriately penalize `trainZ`'s naivete. As shown in Appendix B, `trainZ` has identical $ZPEAK$ and $ZWEIGHT$ values for every galaxy, and thus the photo- z point estimates are constant as a function of true redshift, i. e. a horizontal line at the mode and mean of the training set distribution respectively. The explicit dependence on the individual posteriors in the calculation of the CDE loss, described in Section 5.2, distinguishes this metric from those of the photo- z PDF ensemble and stacked estimator of the redshift distribution, despite their prevalence in the photo- z literature.

In summary, context is crucial to defend against deceptively strong performers such as `trainZ`; **the best photo- z PDF method is the one that most effectively achieves our science goals**, not the one that performs best on a metric that does not reflect those goals. In the absence of a single scientific motivation or the information necessary for a principled metric definition, we must consider many metrics and be critical of the information transmitted by each.

6.2 Extensions to the experimental design

The work presented in this paper is only a first step in assessing photo- z PDF approaches and moving toward an improved photometric redshift estimator. Here we discuss the next steps for subsequent investigations.

This initial paper explores photo- z PDF code perfor-

bles. (The CDE Loss metric of section 4.2 is an exception to this rule.) A lack of appropriate metrics more sophisticated than the CDE Loss remains an open issue for science cases requiring accurate individual galaxy PDFs. The metric-specific performance demonstrated in this paper implies that we may need multiple photo- z PDF approaches tuned to each metric in order to maximize returns over all science cases in large upcoming surveys.

The `trainZ` estimator of Section 3.3, which assigns every galaxy a photo- z PDF equal to $N(z)$ of the training set, is introduced as an experimental control or null test to demonstrate this point via *reductio ad absurdum*. Because our training set is perfectly representative of the test set, $N(z)$ should be identical for both sets down to statistical noise. **We make the alarming observation that `trainZ`, the experimental control, outperforms all codes on the CDF-based metrics, and all but one code on the**

mance in idealized conditions with perfect catalog-based photometry and representative training data, but the resilience of each code to such realistic imperfections in prior information has not yet been evaluated. A top priority for a follow-up study is to test realistic forms of incomplete, erroneous, and non-representative template libraries and training sets as well as the impact of other forms of external priors that must be ingested by the codes, major concerns in Newman et al. (2015); Masters et al. (2017). Outright redshift failures due to emission line misidentification or noise spikes may be modeled by the inclusion of a small number of high-confidence yet false redshifts. We plan to perform a full sensitivity analysis on a realistically incomplete training set of spectroscopic galaxies, modeling the performance of spectrographs, emission-line properties, and expected signal-to-noise to determine which potential training set galaxies are most likely to be excluded.

Appendix A only addresses the stacked estimator of the redshift distribution of the entire galaxy catalogue rather than subsets in bins, tomographic or otherwise. The effects of tomographic binning scheme will be explored in a dedicated future paper, including propagation of redshift uncertainties in a set of fiducial tomographic redshift bins in order to estimate impact on cosmological parameter estimation.

Sequels to this study will also address some shortcomings of our experimental procedure. The fixed redshift grid shared between the codes may have unfairly penalized codes with a different native parameterization, as precision is lost when converting between formats. Performance on the (admittedly small) population of sharply peaked photo-z PDFs may have been suppressed across all codes due to the insufficient resolution of the redshift grid. In light of the results of Malz et al. (2018), in future analyses we plan to switch from a fixed grid to the quantile parameterization or to permit each code to use its native storage format under a shared number of parameters.

Section 4 discussed the difficulty in evaluating PDF accuracy for individual objects. In a follow-up study, we will generate “true PDF” distributions, yielding a dataset that enables a test of PDF accuracy for individual galaxies rather than solely ensembles.

6.3 Realistic mock data

To make optimal use of the LSST data for cosmological and other astrophysical analyses of the LSST-DESC Science Roadmap, future investigations that build upon this one will require a more sophisticated set of galaxy photometry and redshifts. This initial paper explored a data set that was constructed at the catalog level, with no inclusion of the complications that come from measuring photometry from images. Future data challenges will move to catalogs constructed from mock images, including the complications of deblending, sensor inefficiencies, and heterogeneous observing conditions, all anticipated to affect the measured colours of LSST’s galaxy sample (Dawson et al. 2016).

The DC1 galaxy SEDs were linear combinations of just five basis SED templates, but a next generation of data for photo-z PDF investigations must include a broader range of physical properties. Though we only considered $z < 2$ here, LSST 10-year data will contain $z > 2$ galaxies, plagued by fainter apparent magnitudes and anomalous colours due to

stellar evolution. A subsequent study must also have a data set that includes low-level active galactic nuclei (AGN) features in the SEDs, which perturb colours and other host galaxy properties. An observational degeneracy between the Lyman break of a $z \sim 2 - 3$ galaxy from the Balmer break of a $z \sim 0.2 - 0.3$ galaxy is a known source of catastrophic outliers (Massarotti et al. 2001) that was not effectively included in this study. To gauge the sensitivity of photo-z PDF estimators to catastrophic outliers, our data set must include realistic high-redshift galaxy populations.

The overarching plan describing everything laid out in this section is described in more detail in the LSST-DESC Science Roadmap (see Footnote in Section 1).

7 CONCLUSION

This paper compares twelve photo-z PDF codes under controlled experimental conditions of representative and complete prior information to set a baseline for an upcoming sensitivity analysis. This work isolates the impact on metrics of photo-z PDF accuracy due to the estimation technique as opposed to the complications of realistic physical systematics of the photometry. Though the mock data set of this investigation did not include true photo-z posteriors for comparison, **we interpret deviations from perfect results given perfect prior information as the imprint of the implicit assumptions underlying the estimation approach.**

We evaluate the twelve codes under science-agnostic metrics both established and emerging to stress-test the ensemble properties of photo-z PDF catalogues derived by each method. In appendices, we also present metrics of point estimates and a prevalent summary statistic of photo-z PDF catalogues used in cosmological analyses to enable the reader to relate this work to studies of similar scope. We observe that no one code dominates in all metrics, and that the standard metrics of photo-z PDFs and the stacked estimator of the redshift distribution can be gamed by a very simplistic procedure that asserts the prior over the data. We emphasize to the photo-z community that **metrics used to vet photo-z PDF methods must be scrutinized to ensure they correspond to the quantities that matter to our science.**

Acknowledgments

Author contributions are listed below.
S.J. Schmidt: Co-led the project. (conceptualization, data curation, formal analysis, investigation, methodology, project administration, resources, software, supervision, visualization, writing – original draft, writing – review & editing)

A.I. Malz: Co-led the project, contributed to choice of metrics, implementation in code, and writing. (conceptualization, methodology, project administration, resources, software, visualization, writing – original draft, writing – review & editing)

J.Y.H. Soo: Ran ANNz2 and Delight, updated abstract, edited sections 1 through 6, added tables in Methods and Results, updated references.bib and added references throughout the paper

1160 I.A. Almosallam: vetted the early versions of the data set 1222
 1161 and ran many photo-z codes on it, applied GPz to the final 1223
 1162 version and wrote the GPz subsection 1224
 1163 M. Brescia: main ideator of METAPHOR and of MLPQNA; 1225
 1164 modification of METAPHOR pipeline to fit the LSST data 1226
 1165 structure and requirements 1227
 1166 S. Cavaudi: Contributed to choice and test of metrics, ran 1228
 1167 METAPHOR, minor text editing 1229
 1168 J. Cohen-Tanugi: contributed to running code, analysis 1230
 1169 discussion, and editing, reviewing the paper 1231
 1170 A.J. Connolly: Developed the colour-matched nearest- 1232
 1171 neighbours photo-z code; participated in discussions of the 1233
 1172 analysis. 1234
 1173 P.E. Freeman: Contributed to choice of CDE metrics and 1235
 1174 to implementation of FlexZBoost 1236
 1175 M.L. Graham: Ran the colour-matched nearest-neighbours 1237
 1176 photo-z code on the Buzzard catalog and wrote the relevant 1238
 1177 piece of Section 2; participated in discussions of the analysis. 1239
 1178 K. Iyer: assisted in writing metric functions used to evaluate 1240
 1179 codes 1241
 1180 M.J. Jarvis: Contributed text on AGN to Discussion section 1242
 1181 and portions of GPz work 1243
 1182 J.B. Kalmbach: Worked on preparing the figures for the 1244
 1183 paper.
 1184 E. Kovacs: Ran simulations, discussed data format and 1245
 1185 properties for SEDs, dust, and ELG corrections
 1186 A.B. Lee: Co-developed FlexZBoost and the CDE loss 1246
 1187 statistic, wrote text on the work, and supervised the 1247
 1188 development of FlexZBoost software packages 1248
 1189 G. Longo: Scientific advise, test and validation of the 1249
 1190 modified METAPHOR pipeline, text of the METAPHOR 1249
 1191 section 1250
 1192 C. B. Morrison: Managerial support; Discussions with au- 1251
 1193 thors regarding metrics and style; Some coding contribution 1252
 1194 to metric computation. 1253
 1195 J. Newman: Contributions to overall strategy, design of 1254
 1196 metrics, and supervision of work done by Rongpu Zhou 1255
 1197 E. Nourbakhsh: Ran and optimized TPZ code and wrote a 1256
 1198 subsection of Section 2 for TPZ 1257
 1199 E. Nuss: contributed to running code, analysis discussion, 1258
 1200 and editing, reviewing the paper 1259
 1201 T. Pospisil: Co-developed FlexZBoost software and CDE 1260
 1202 loss calculation code 1261
 1203 H. Tranin: contributed to providing SkyNet results and 1262
 1204 writing the relevant section 1263
 1205 R. Zhou: Optimized and ran EAZY and contributed to the 1264
 1206 draft 1265
 1207 R. Izbicki: Co-developed FlexZBoost and the CDE loss 1266
 1208 statistic, and wrote software for FlexZBoost 1267
 1209
 1210 The authors would like to thank their LSST-DESC pub- 1267
 1211 lication review committee for comments that improved the 1268
 1212 paper draft.

1213 personal funding sources SJS acknowledges support 1269
 1214 from DOE grant DE-SC0009999 and NSF/AURA grant 1269
 1215 N56981C. AIM acknowledges support from the Max Planck 1270
 1216 Society and the Alexander von Humboldt Foundation in the 1271
 1217 framework of the Max Planck-Humboldt Research Award 1271
 1218 endowed by the Federal Ministry of Education and Research. 1272
 1219 During the completion of this work, AIM was advised by 1273
 1220 David W. Hogg and was supported by National Science 1274
 1221 Foundation grant AST-1517237. 1275

In addition to packages cited in the text, analyses performed in this paper used the following software packages: `Numpy` and `Scipy` (Oliphant 2007), `Matplotlib` (Hunter 2007), `Seaborn` (Waskom et al. 2017), `minFunc` (Schmidt 2005), `qp` (Malz & Marshall 2018; Malz et al. 2018), `pySkyNet` (Bonnett 2016), and `photUtils` from the LSST simulations package (Connolly et al. 2014).

The DESC acknowledges ongoing support from the Institut National de Physique Nucléaire et de Physique des Particules in France; the Science & Technology Facilities Council in the United Kingdom; and the Department of Energy, the National Science Foundation, and the LSST Corporation in the United States. DESC uses resources of the IN2P3 Computing Center (CC-IN2P3-Lyon/Villeurbanne - France) funded by the Centre National de la Recherche Scientifique; the National Energy Research Scientific Computing Center, a DOE Office of Science User Facility supported by the Office of Science of the U.S. Department of Energy under Contract No. DE-AC02-05CH11231; STFC DiRAC HPC Facilities, funded by UK BIS National E-infrastructure capital grants; and the UK particle physics grid, supported by the GridPP Collaboration. This work was performed in part under DOE Contract DE-AC02-76SF00515.

APPENDIX A: EVALUATION OF THE REDSHIFT DISTRIBUTION

Perhaps the most popular application of photo-z PDFs is the estimation of the overall redshift distribution $N(z)$, a quantity that enters some cosmological calculations and the true value of which is known for the DC1 data set and will be denoted as $\hat{N}(z)$. In terms of the prior information provided to each method, the true redshift distribution satisfies the tautology $\hat{N}(z) = p(z|I_D)$ due to our experimental set-up; because the DC1 training and template sets are representative and complete, I_D represents a prior that is also equal to the truth. In this ideal case of complete and representative prior information, the method that would give the best approximation to $\hat{N}(z)$ would be one that neglects all the information contained in the photometry $\{d_i\}_{N_{tot}}$ and gives every galaxy the same photo-z PDF $\hat{p}_i(z) = \hat{N}(z)$ for all i ; the inclusion of any information from the photometry would only introduce noise to the optimal result of returning the prior. This is the exact estimator, `trainZ`, that we have described in Section 3.3, and which will serve as an experimental control.

A1 Metrics of the stacked estimator of the redshift distribution

“Stacking” according to

$$\hat{N}^H(z) \equiv \frac{1}{N_{tot}} \sum_i^{N_{tot}} \hat{p}_i^H(z) \quad (\text{A1})$$

is the most widely accepted method for obtaining $\hat{N}^H(z)$ as an estimator of the redshift distribution from photo-z PDFs derived by a method H . Though the use of the stacked estimator of the redshift distribution is not formally correct (Malz & Hogg prep), we use it under the untested assumption that the response of our metrics of $\hat{N}^H(z)$ will be anal-

ogous to the same metrics applied to a principled estimator of the redshift distribution.

As $N(z)$ is itself a univariate PDF, we apply the metrics of the previous sections to it as well. We additionally calculate the first three moments

$$\langle z^m \rangle \equiv \int_{-\infty}^{\infty} z^m N(z) dz \quad (\text{A2})$$

of the estimated redshift distribution $\hat{N}^H(z)$ for each code and compare them to the moments of the true redshift distribution $\tilde{N}(z)$. Under the assumption that the stacked estimator is unbiased, a superior method minimizes the difference between the true and estimated moments.

A2 Performance on the stacked estimator of the redshift distribution

Figure A1 shows the stacked estimator $\hat{N}(z)$ of the redshift distribution for each code compared to the true redshift distribution $\tilde{N}(z)$, where the stacked estimator has been smoothed for each code in the plot using a kernel density estimate (KDE) with a bandwidth chosen by Scott’s Rule (Scott 1992) in order to minimize visual differences in small-scale features; the quantitative statistics, however, are calculated using the empirical CDF which is not smoothed.

Many of the codes, including all the model-fitting approaches and ANNz2, GPz, METAPhR, and SkyNet from the data-driven camp, overestimate the redshift density at $z \sim 1.4$. This behavior is a consequence of the 4000 Åbreak passing through the gap between the z and y filters, which induces a genuine discontinuity in the $z-y$ colour as a function of redshift that can sway the photo- z PDF estimates in the absence of bluer spectral features.

ANNz2, GPz, and METAPhR feature exaggerated peaks and troughs relative to the training set, a potential sign of overtraining. Further investigation on overtraining is needed, if present this is an obstacle that may be overcome with adjustment of the implementation.

As expected, trainZ perfectly recovers the true redshift distribution: as the training sample is selected from the same underlying distribution as the test set, the redshift distributions are identical, up to Poisson fluctuations due to the finite number of sample galaxies. CMNN is also in excellent agreement for similar reasons: with a representative training sample of galaxies spanning the colour-space, the sum of the colour-matched neighbour redshifts should return the true redshift distribution. FlexZBoost and TPZ also perform superb recovery of the true redshift distribution, with only a slight deviation at $z \sim 1.4$. Our metrics, however, cannot discern whether these four approaches, as well as Delight, are spared the $z \sim 1.4$ degeneracy in $\hat{N}(z)$ because they have more effectively used information in the data or if the impact is simply washed out by the stacked estimator’s effective average over the test set galaxy sample. See Appendix B for further discussion of the $z \sim 1.4$ issue.

Figure A2 shows the quantitative Kolmogorov-Smirnov (KS), Cramer-Von Mises (CvM), and Anderson Darling (AD) test statistics for each of the codes for the $\hat{N}(z)$ based measures. The horizontal lines show the result of a bootstrap resampling of the training set using 30,000 samples for trainZ, representing a conservative idealized limit on expected performance for a modest-sized representative train-

Table A1. Moments of the stacked estimator $\hat{N}(z)$ of the redshift distribution. Most of the codes considered recover the moments of $\tilde{N}(z)$

Moments of $\hat{N}(z)$			
Estimator	mean	variance	skewness
Empirical “truth”	0.701	0.630	0.671
ANNz2	0.702	0.625	0.653
BPZ	0.699	0.629	0.671
Delight	0.692	0.609	0.638
EAZY	0.681	0.595	0.619
FlexZBoost	0.694	0.610	0.631
GPz	0.696	0.615	0.639
LePhare	0.718	0.668	0.741
METAPhR	0.705	0.628	0.657
CMNN	0.701	0.628	0.667
SkyNet	0.743	0.708	0.797
TPZ	0.700	0.619	0.643
trainZ	0.699	0.627	0.666

ing set of galaxies, as mentioned in Section 5.1. The AD bootstrap statistic is elevated due to its sensitivity to the tails of distributions. The stacked estimators of the redshift distribution for CMNN and trainZ best estimate $\tilde{N}(z)$ under these metrics, whereas EAZY, LePhare, METAPhR, and SkyNet underperform; BPZ, GPz, and TPZ are within a factor of two of the conservative limit for all statistics. It is unsurprising that CMNN scores well, as with a nearly complete and representative training set choosing neighbouring points in color/magnitude space to construct an estimator should lead to excellent agreement in the final $\hat{N}(z)$.

It is, however, surprising that TPZ does well on $\hat{N}(z)$ given its poor performance on the ensemble photo- z PDFs, especially knowing that TPZ was optimized for photo- z PDF ensemble metrics rather than the stacked estimator of the redshift distribution. A possible explanation is the choice of smoothing parameter chosen during validation, which affects photo- z PDF widths as well as overall redshift bias and could be modified to improve performance under the photo- z PDF metrics.

The first three moments of the stacked $\hat{N}(z)$ distribution relative to the empirical estimate of the truth distribution are given in Table A1. Accuracy of the moments varies widely between codes, raising concerns about the propagation to cosmological analyses.

SkyNet exhibits redshift bias in Figure A1 and is a clear outlier in the first moment of $\hat{N}(z)$ in Table A1. The SkyNet algorithm employs a random subsampling of the training set without testing that the subset is representative of the full population, and the implementation used here does not upweight rarer low- and high-redshift galaxies, as in Bonnett (2015), suggesting a possible cause that may be addressed in future work.

APPENDIX B: Photo- z POINT ESTIMATION AND METRICS

While this work assumes that science applications value the information of the full photo- z PDF, we present conventional metrics of photo- z point estimates as a quick and dirty vi-

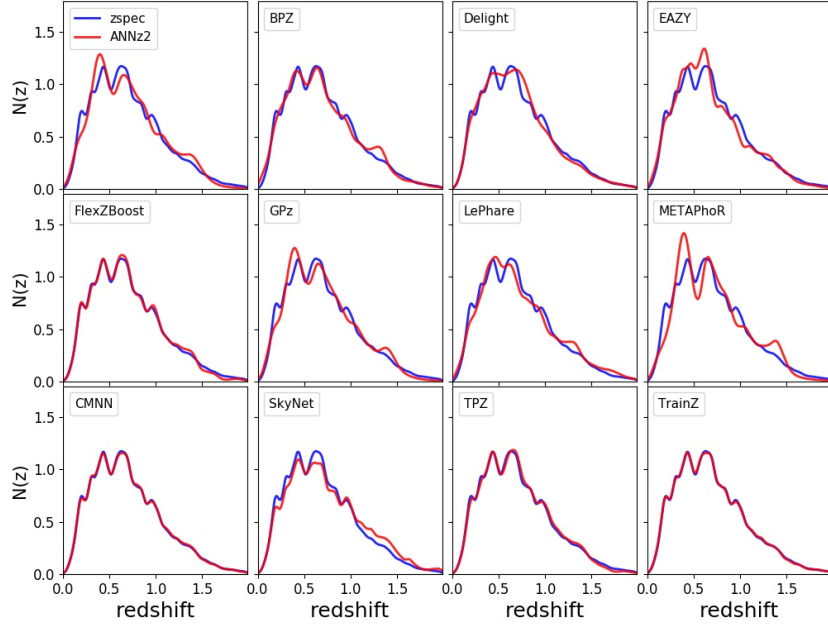


Figure A1. The smoothed stacked estimator $\hat{N}(z)$ of the redshift distribution (red) produced by each code (panels) compared to the true redshift distribution $\tilde{N}(z)$ (blue). Varying levels of agreement are seen among the codes, with the smallest deviations for CMNN, FlexZBoost, TPZ, and trainZ.

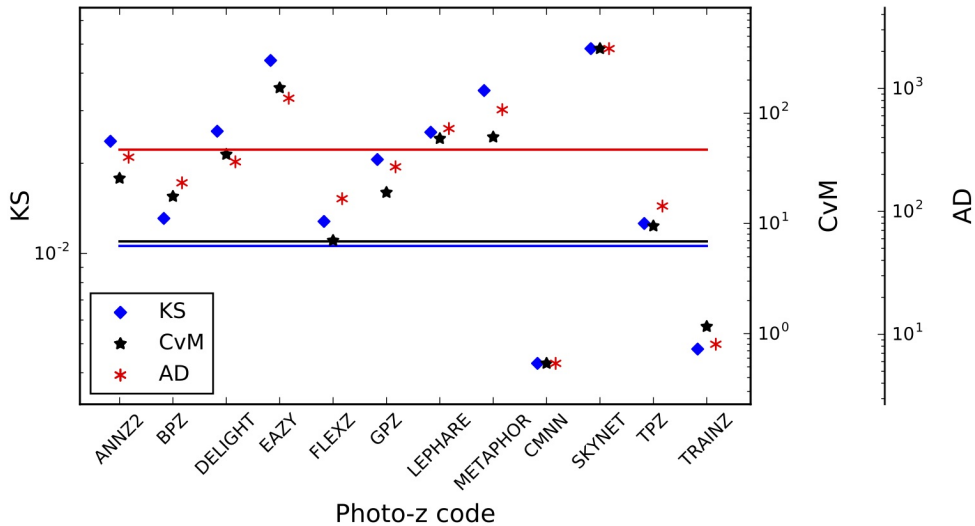


Figure A2. A visualization of the Kolmogorov-Smirnov (KS, blue diamond), Cramer-von Mises (CvM, black star), and Anderson-Darling (AD, red asterisk) statistics for the $\hat{N}(z)$ distributions. Horizontal lines indicate the statistic values (including uncertainty) achieved using trainZ via bootstrap resampling a training set containing 30,000 redshifts. We make the reassuring observation that these related statistics do not disagree significantly with one another. CMNN outperforms the control case, trainZ, and several codes are within a factor of two of this conservative idealized limit. SkyNet scores poorly due to an overall bias in its redshift predictions.

1372 dual diagnostic tool and to facilitate direct comparisons to 1374 historical studies.

B1 Reduction of photo-z PDFs to point estimates

1375 Though we acknowledge that many of the codes can also
 1376 return a native photo-z point estimate, we put all codes on
 1377 equal footing by considering two generic photo-z point es-
 1378 timators, the mode z_{PEAK} and main-peak-mean z_{WEIGHT}

- 1379 (Dahlen et al. 2013), a weighted mean within the bounds of 1431
 1380 the main peak, as identified by the roots of $p(z) - 0.05 \times 1432$
 1381 z_{PEAK} . Though z_{WEIGHT} neglects information in a sec- 1433
 1382 ondary peak of e. g. a bimodal distribution, it avoids the 1434
 1383 pitfall of reducing the photo-z PDF to a redshift between 1435
 1384 peaks where there is low probability. 1436
- 1385 **B2 Metrics of photo-z point estimates** 1437
- 1386 We calculate the commonly used point estimate metrics of 1441
 1387 the overall intrinsic scatter, bias, and catastrophic outlier 1442
 1388 rate, defined in terms of the standard error $e_z \equiv (z_{PEAK} - 1443$
 1389 $z_{true})/(1 + z_{true})$. Because the standard deviation of the 1444
 1390 photo-z residuals is sensitive to outliers, we define the scat- 1445
 1391 ter in terms of the Interquartile Range (IQR), the difference 1446
 1392 between the 75th and 25th percentiles of the distribution of 1447
 1393 e_z , imposing the scaling $\sigma_{IQR} = IQR/1.349$ to ensure that 1448
 1394 the area within σ_{IQR} is the same as that within one standard 1449
 1395 deviation from a standard Normal distribution. We also re- 1450
 1396 sist the effect of catastrophic outliers by defining the bias 1451
 1397 b_z as the median rather than mean value of e_z . The cata- 1452
 1398 strophic outlier rate f_{out} is defined as the fraction of galaxies 1453
 1399 with e_z greater than $\max(3\sigma_{IQR}, 0.06)$. 1454
- 1400 For reference, Section 3.8 of the LSST Science Book 1456
 1401 (Abell et al. 2009) uses the standard definitions of these 1457
 1402 parameters in requiring 1458
- 1403 • RMS scatter $\sigma < 0.02(1 + z_{true})$ 1459
 - 1404 • bias $b_z < 0.003$ 1460
 - 1405 • catastrophic outlier rate $f_{out} < 10\%$. 1461
- 1406 **B3 Comparison of photo-z point estimate metrics** 1462
- 1407 Figure B1 shows both point estimates for all codes both 1463
 1408 z_{PEAK} and z_{WEIGHT} . Point density is shown with mixed 1464
 1409 contours to emphasize that most of the galaxies do fall close 1465
 1410 to the $z_{phot} = z_{spec}$ line, while points trace the details of the 1466
 1411 catastrophic outlier populations. 1467
- 1412 The finite grid spacing of the photo-z PDFs induces 1468
 1413 some discretization in z_{PEAK} . The features perpendicular 1469
 1414 to the $z_{phot} = z_{spec}$ line are due to the 4000 Åbreak pass- 1470
 1415 ing through the gaps between adjacent filters. Even the 1471
 1416 strongest codes feature populations far from the $z_{phot} = 1472$
 1417 z_{spec} line representing a degeneracy in the space of colours 1473
 1418 and redshifts. 1474
- 1419 The intrinsic scatter, bias, and catastrophic outlier rate 1475
 1420 are given in Table B1. Perhaps unsurprisingly, performance 1476
 1421 under these metrics largely tracks that of the metrics of Sec- 1477
 1422 tion 4 of the photo-z PDFs from which the point estimates 1478
 1423 were derived. All twelve codes perform at or near the goals 1479
 1424 of the LSST Science Requirements Document¹⁸ and Gra- 1480
 1425 ham et al. (2018), which is encouraging if not unexpected 1481
 1426 for $i < 25.3$. 1482
- 1427 **REFERENCES**
- 1428 Abbott T., et al., 2005, preprint (arXiv:astro-ph/0510346)
 1429 Abell P. A., et al., 2009, preprint (arXiv:0912.0201),
 1430 Aihara H., et al., 2018a, *PASJ*, **70**, S4
- Aihara H., et al., 2018b, *PASJ*, **70**, S8
 Almosallam I. A., Lindsay S. N., Jarvis M. J., Roberts S. J., 2016a, *MNRAS*, **455**, 2387
 Almosallam I. A., Jarvis M. J., Roberts S. J., 2016b, *MNRAS*, **462**, 726
 Arnouts S., Cristiani S., Moscardini L., Matarrese S., Lucchin F., Fontana A., Giallongo E., 1999, *MNRAS*, **310**, 540
 Behroozi P. S., Wechsler R. H., Wu H.-Y., 2013, *ApJ*, **762**, 109
 Benítez N., 2000, *ApJ*, **536**, 571
 Bernstein G., Huterer D., 2010, *MNRAS*, **401**, 1399
 Blanton M. R., Roweis S., 2007, *AJ*, **133**, 734
 Blanton M. R., et al., 2005, *AJ*, **129**, 2562
 Bonnett C., 2015, *MNRAS*, **449**, 1043
 Bonnett C., 2016, Python wrapper to SkyNet, <https://pyskynet.readthedocs.io/en/latest/>
 Bonnett C., et al., 2016, *Phys. Rev. D*, **94**, 042005
 Bordoloi R., Lilly S. J., Amara A., 2010, *MNRAS*, **406**, 881
 Brammer G. B., van Dokkum P. G., Coppi P., 2008, *ApJ*, **686**, 1503
 Breiman L., Friedman J. H., Olshen R. A., Stone C. J., 1984, Classification and Regression Trees, Statistics/Probability Series. Wadsworth Publishing Company, Belmont, California, U.S.A
 Brescia M., Cavuoti S., Amaro V., Riccio G., Angora G., Vellucci C., Longo G., 2018, preprint, ([arXiv:1802.07683](https://arxiv.org/abs/1802.07683))
 Carrasco Kind M., Brunner R. J., 2013, *MNRAS*, **432**, 1483
 Carrasco Kind M., Brunner R. J., 2014, *MNRAS*, **442**, 3380
 Cavuoti S., Amaro V., Brescia M., Vellucci C., Tortora C., Longo G., 2017, *MNRAS*, **465**, 1959
 Chen T., Guestrin C., 2016, in Proceedings of the 22Nd ACM SIGKDD International Conference on Knowledge Discovery and Data Mining. KDD '16. ACM, New York, NY, USA, pp 785–794, doi:[10.1145/2939672.2939785](https://doi.org/10.1145/2939672.2939785), <http://doi.acm.org/10.1145/2939672.2939785>
 Connolly A. J., et al., 2014, in Angeli G. Z., Dierickx P., eds, Society of Photo-Optical Instrumentation Engineers (SPIE) Conference Series Vol. 9150, Modeling, Systems Engineering, and Project Management for Astronomy VI. p. 14, doi:[10.1117/12.2054953](https://doi.org/10.1117/12.2054953)
 Dahlen T., et al., 2013, *ApJ*, **775**, 93
 Dawson W. A., Schneider M. D., Tyson J. A., Jee M. J., 2016, *ApJ*, **816**, 11
 DeRose J., et al., 2019, arXiv e-prints, p. [arXiv:1901.02401](https://arxiv.org/abs/1901.02401)
 Erben T., et al., 2013, *MNRAS*, **433**, 2545
 Fernández-Soto A., Lanzetta K. M., Yahil A., 1999, *ApJ*, **513**, 34
 Firth A. E., Lahav O., Somerville R. S., 2003, *MNRAS*, **339**, 1195
 Freeman P. E., Izbicki R., Lee A. B., 2017, *MNRAS*, **468**, 4556
 Graff P., Feroz F., Hobson M. P., Lasenby A., 2014, *MNRAS*, **441**, 1741
 Graham M. L., Connolly A. J., Ivezic Ž., Schmidt S. J., Jones R. L., Jurić M., Daniel S. F., Yoachim P., 2018, *AJ*, **155**, 1
 Green J., et al., 2012, preprint (arXiv:1208.4012),
 Hildebrandt H., et al., 2010, *A&A*, **523**, A31
 Hofmann B., Mathé P., 2018, *Inverse Problems*, **34**, 015007
 Hunter J. D., 2007, Matplotlib: A 2D Graphics Environment, doi:[10.1109/MCSE.2007.55](https://doi.org/10.1109/MCSE.2007.55)
 Ilbert O., et al., 2006, *A&A*, **457**, 841
 Ivezic Ž., et al., 2008, preprint (arXiv:0805.2366),
 Izbicki R., Lee A. B., 2017, *Electron. J. Statist.*, **11**, 2800
 Izbicki R., Lee A. B., Freeman P. E., 2017, *Ann. Appl. Stat.*, **11**, 698
 Laureijs R., et al., 2011, preprint (1110.3193),
 Leistedt B., Hogg D. W., 2017, *ApJ*, **838**, 5
 Malz A., Hogg D., in prep., CHIPPR, chippr, <https://github.com/aimalz/chippr>
 Malz A., Marshall P., 2018, qp: Quantile parametrization for probability distribution functions (ascl:1809.011)
 Malz A. I., Marshall P. J., DeRose J., Graham M. L., Schmidt

¹⁸ available at: <http://ls.st/srd>

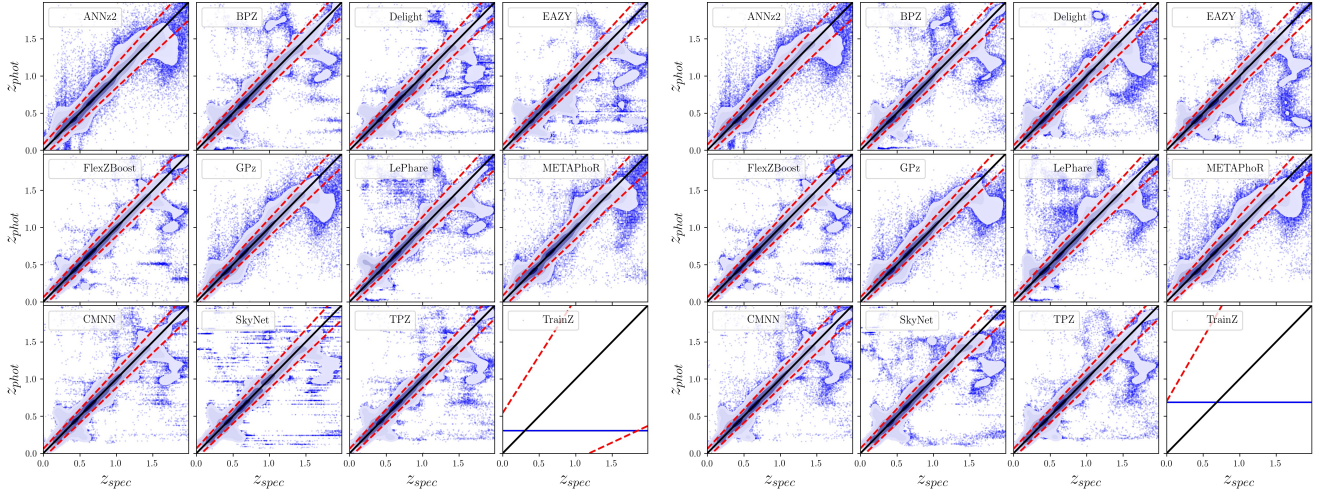


Figure B1. The density of photo- z point estimates (contours) reduced from the photo- z PDFs with outliers (blue) beyond the outlier cutoff (red dashed lines), via the mode (z_{PEAK} , left panel) and main-peak-mean (z_{WEIGHT} , right panel). The **trainZ** estimator (lower right sub-panels) has a shared z_{PEAK} and z_{WEIGHT} for the entire test set galaxy sample.

Table B1. Photo- z point estimate statistics

Photo- z PDF Code	Z_{PEAK}		Z_{WEIGHT}			
	$\frac{\sigma_{IQR}}{(1+z)}$	median	outlier fraction	$\frac{\sigma_{IQR}}{(1+z)}$	median	outlier fraction
ANNz2	0.0270	0.00063	0.044	0.0244	0.000307	0.047
BPZ	0.0215	-0.00175	0.035	0.0215	-0.002005	0.032
Delight	0.0212	-0.00185	0.038	0.0216	-0.002158	0.038
EAZY	0.0225	-0.00218	0.034	0.0226	-0.003765	0.029
FlexZBoost	0.0154	-0.00027	0.020	0.0148	-0.000211	0.017
GPz	0.0197	-0.00000	0.052	0.0195	0.000113	0.051
LePhare	0.0236	-0.00161	0.058	0.0239	-0.002007	0.056
METAPhoR	0.0264	0.00000	0.037	0.0262	0.001333	0.048
CMNN	0.0184	-0.00132	0.035	0.0170	-0.001049	0.034
SkyNet	0.0219	-0.00167	0.036	0.0218	0.000174	0.037
TPZ	0.0161	0.00309	0.033	0.0166	0.003048	0.031
trainZ	0.1808	-0.2086	0.000	0.2335	0.022135	0.000

- 1498 S. J., Wechsler R., (LSST Dark Energy Science Collaboration 1519
 1499 2018, *AJ*, **156**, 35 1520
 1500 Mandelbaum R., et al., 2008, *MNRAS*, **386**, 781 1521
 1501 Massarotti M., Iovino A., Buzzoni A., 2001, *A&A*, **368**, 74 1522
 1502 Masters D. C., Stern D. K., Cohen J. G., Capak P. L., Rhodes 1523
 1503 J. D., Castander F. J., Paltani S., 2017, *ApJ*, **841**, 111 1524
 1504 Newman J. A., et al., 2015, *Astroparticle Physics*, **63**, 81 1525
 1505 Oliphant T., 2007, Python for Scientific Computing, 1526
 1506 doi:10.1109/MCSE.2007.58 1527
 1507 Oyaizu H., Lima M., Cunha C. E., Lin H., Frieman J., 2008, *ApJ*, 1528
 1508 **689**, 709 1529
 1509 Polsterer K. L., D'Isanto A., Gieseke F., 2016, preprint 1530
 1510 (arXiv:1608.08016), 1531
 1511 Rasmussen C., Williams C., 2006, Gaussian Processes for Machine 1532
 1512 Learning. Adaptative computation and machine learning se- 1533
 1513 ries, MIT Press, Cambridge, MA 1534
 1514 Rau M. M., Seitz S., Brimioule F., Frank E., Friedrich O., Gruen 1535
 1515 D., Hoyle B., 2015, *MNRAS*, **452**, 3710 1536
 1516 Reddick R. M., Wechsler R. H., Tinker J. L., Behroozi P. S., 2013, 1517
 1517 *ApJ*, **771**, 30
 1518 Sadeh I., Abdalla F. B., Lahav O., 2016, *PASP*, **128**, 104502 1519
 1520
 1521
 1522
 1523
 1524
 1525
 1526
 1527
 1528
 1529
 1530
 1531
 1532
 1533
 1534
 1535
 1536
 1537
 1538
 1539
 1540
 1541
 1542
 1543
 1544
 1545
 1546
 1547
 1548
 1549
 1550
 1551
 1552
 1553
 1554
 1555
 1556
 1557
 1558
 1559
 1560
 1561
 1562
 1563
 1564
 1565
 1566
 1567
 1568
 1569
 1570
 1571
 1572
 1573
 1574
 1575
 1576
 1577
 1578
 1579
 1580
 1581
 1582
 1583
 1584
 1585
 1586
 1587
 1588
 1589
 1590
 1591
 1592
 1593
 1594
 1595
 1596
 1597
 1598
 1599
 1600
 1601
 1602
 1603
 1604
 1605
 1606
 1607
 1608
 1609
 1610
 1611
 1612
 1613
 1614
 1615
 1616
 1617
 1618
 1619
 1620
 1621
 1622
 1623
 1624
 1625
 1626
 1627
 1628
 1629
 1630
 1631
 1632
 1633
 1634
 1635
 1636
 1637
 1638
 1639
 1640
 1641
 1642
 1643
 1644
 1645
 1646
 1647
 1648
 1649
 1650
 1651
 1652
 1653
 1654
 1655
 1656
 1657
 1658
 1659
 1660
 1661
 1662
 1663
 1664
 1665
 1666
 1667
 1668
 1669
 1670
 1671
 1672
 1673
 1674
 1675
 1676
 1677
 1678
 1679
 1680
 1681
 1682
 1683
 1684
 1685
 1686
 1687
 1688
 1689
 1690
 1691
 1692
 1693
 1694
 1695
 1696
 1697
 1698
 1699
 1700
 1701
 1702
 1703
 1704
 1705
 1706
 1707
 1708
 1709
 1710
 1711
 1712
 1713
 1714
 1715
 1716
 1717
 1718
 1719
 1720
 1721
 1722
 1723
 1724
 1725
 1726
 1727
 1728
 1729
 1730
 1731
 1732
 1733
 1734
 1735
 1736
 1737
 1738
 1739
 1740
 1741
 1742
 1743
 1744
 1745
 1746
 1747
 1748
 1749
 1750
 1751
 1752
 1753
 1754
 1755
 1756
 1757
 1758
 1759
 1760
 1761
 1762
 1763
 1764
 1765
 1766
 1767
 1768
 1769
 1770
 1771
 1772
 1773
 1774
 1775
 1776
 1777
 1778
 1779
 1780
 1781
 1782
 1783
 1784
 1785
 1786
 1787
 1788
 1789
 1790
 1791
 1792
 1793
 1794
 1795
 1796
 1797
 1798
 1799
 1800
 1801
 1802
 1803
 1804
 1805
 1806
 1807
 1808
 1809
 1810
 1811
 1812
 1813
 1814
 1815
 1816
 1817
 1818
 1819
 1820
 1821
 1822
 1823
 1824
 1825
 1826
 1827
 1828
 1829
 1830
 1831
 1832
 1833
 1834
 1835
 1836
 1837
 1838
 1839
 1840
 1841
 1842
 1843
 1844
 1845
 1846
 1847
 1848
 1849
 1850
 1851
 1852
 1853
 1854
 1855
 1856
 1857
 1858
 1859
 1860
 1861
 1862
 1863
 1864
 1865
 1866
 1867
 1868
 1869
 1870
 1871
 1872
 1873
 1874
 1875
 1876
 1877
 1878
 1879
 1880
 1881
 1882
 1883
 1884
 1885
 1886
 1887
 1888
 1889
 1890
 1891
 1892
 1893
 1894
 1895
 1896
 1897
 1898
 1899
 1900
 1901
 1902
 1903
 1904
 1905
 1906
 1907
 1908
 1909
 1910
 1911
 1912
 1913
 1914
 1915
 1916
 1917
 1918
 1919
 1920
 1921
 1922
 1923
 1924
 1925
 1926
 1927
 1928
 1929
 1930
 1931
 1932
 1933
 1934
 1935
 1936
 1937
 1938
 1939
 1940
 1941
 1942
 1943
 1944
 1945
 1946
 1947
 1948
 1949
 1950
 1951
 1952
 1953
 1954
 1955
 1956
 1957
 1958
 1959
 1960
 1961
 1962
 1963
 1964
 1965
 1966
 1967
 1968
 1969
 1970
 1971
 1972
 1973
 1974
 1975
 1976
 1977
 1978
 1979
 1980
 1981
 1982
 1983
 1984
 1985
 1986
 1987
 1988
 1989
 1990
 1991
 1992
 1993
 1994
 1995
 1996
 1997
 1998
 1999
 2000
 2001
 2002
 2003
 2004
 2005
 2006
 2007
 2008
 2009
 2010
 2011
 2012
 2013
 2014
 2015
 2016
 2017
 2018
 2019
 2020
 2021
 2022
 2023
 2024
 2025
 2026
 2027
 2028
 2029
 2030
 2031
 2032
 2033
 2034
 2035
 2036
 2037
 2038
 2039
 2040
 2041
 2042
 2043
 2044
 2045
 2046
 2047
 2048
 2049
 2050
 2051
 2052
 2053
 2054
 2055
 2056
 2057
 2058
 2059
 2060
 2061
 2062
 2063
 2064
 2065
 2066
 2067
 2068
 2069
 2070
 2071
 2072
 2073
 2074
 2075
 2076
 2077
 2078
 2079
 2080
 2081
 2082
 2083
 2084
 2085
 2086
 2087
 2088
 2089
 2090
 2091
 2092
 2093
 2094
 2095
 2096
 2097
 2098
 2099
 20100
 20101
 20102
 20103
 20104
 20105
 20106
 20107
 20108
 20109
 20110
 20111
 20112
 20113
 20114
 20115
 20116
 20117
 20118
 20119
 20120
 20121
 20122
 20123
 20124
 20125
 20126
 20127
 20128
 20129
 20130
 20131
 20132
 20133
 20134
 20135
 20136
 20137
 20138
 20139
 20140
 20141
 20142
 20143
 20144
 20145
 20146
 20147
 20148
 20149
 20150
 20151
 20152
 20153
 20154
 20155
 20156
 20157
 20158
 20159
 20160
 20161
 20162
 20163
 20164
 20165
 20166
 20167
 20168
 20169
 20170
 20171
 20172
 20173
 20174
 20175
 20176
 20177
 20178
 20179
 20180
 20181
 20182
 20183
 20184
 20185
 20186
 20187
 20188
 20189
 20190
 20191
 20192
 20193
 20194
 20195
 20196
 20197
 20198
 20199
 20200
 20201
 20202
 20203
 20204
 20205
 20206
 20207
 20208
 20209
 20210
 20211
 20212
 20213
 20214
 20215
 20216
 20217
 20218
 20219
 20220
 20221
 20222
 20223
 20224
 20225
 20226
 20227
 20228
 20229
 20230
 20231
 20232
 20233
 20234
 20235
 20236
 20237
 20238
 20239
 20240
 20241
 20242
 20243
 20244
 20245
 20246
 20247
 20248
 20249
 20250
 20251
 20252
 20253
 20254
 20255
 20256
 20257
 20258
 20259
 20260
 20261
 20262
 20263
 20264
 20265
 20266
 20267
 20268
 20269
 20270
 20271
 20272
 20273
 20274
 20275
 20276
 20277
 20278
 20279
 20280
 20281
 20282
 20283
 20284
 20285
 20286
 20287
 20288
 20289
 20290
 20291
 20292
 20293
 20294
 20295
 20296
 20297
 20298
 20299
 20300
 20301
 20302
 20303
 20304
 20305
 20306
 20307
 20308
 20309
 20310
 20311
 20312
 20313
 20314
 20315
 20316
 20317
 20318
 20319
 20320
 20321
 20322
 20323
 20324
 20325
 20326
 20327
 20328
 20329
 20330
 20331
 20332
 20333
 20334
 20335
 20336
 20337
 20338
 20339
 20340
 20341
 20342
 20343
 20344
 20345
 20346
 20347
 20348
 20349
 20350
 20351
 20352
 20353
 20354
 20355
 20356
 20357
 20358
 20359
 20360
 20361
 20362
 20363
 20364
 20365
 20366
 20367
 20368
 20369
 20370
 20371
 20372
 20373
 20374
 20375
 20376
 20377
 20378
 20379
 20380
 20381
 20382
 20383
 20384
 20385
 20386
 20387
 20388
 20389
 20390
 20391
 20392
 20393
 20394
 20395
 20396
 20397
 20398
 20399
 20400
 20401
 20402
 20403
 20404
 20405
 20406
 20407
 20408
 20409
 20410
 20411
 20412
 20413
 20414
 20415
 20416
 20417
 20418
 20419
 20420
 20421
 20422
 20423
 20424
 20425
 20426
 20427
 20428
 20429
 20430
 20431
 20432
 20433
 20434
 20435
 20436
 20437
 20438
 20439
 20440
 20441
 20442
 20443
 20444
 20445
 20446
 20447
 20448
 20449
 20450
 20451
 20452
 20453
 20454
 20455
 20456
 20457
 20458
 20459
 20460
 20461
 20462
 20463
 20464
 20465
 20466
 20467
 20468
 20469
 20470
 20471
 20472
 20473
 20474
 20475
 20476
 20477
 20478
 20479
 20480
 20481
 20482
 20483
 20484
 20485
 20486
 20487
 20488
 20489
 20490
 20491
 20492
 20493
 20494
 20495
 20496
 20497
 20498
 20499
 20500
 20501
 20502
 20503
 20504
 20505
 20506
 20507
 20508
 20509
 20510
 20511
 20512
 20513
 20514
 20515
 20516
 20517
 20518
 20519
 20520
 20521
 20522